

Topographic asymmetry of the South Atlantic from global models of mantle flow and lithospheric stretching

Nicolas Flament^{a,*}, Michael Gurnis^b, Simon Williams^a, Maria Seton^a, Jakob Skogseid^c, Christian Heine^a, R. Dietmar Müller^a

^aEarthByte Group, School of Geosciences, The University of Sydney, Sydney, NSW 2006, Australia

^bSeismological Laboratory, California Institute of Technology, Pasadena, CA 91125 USA

^cStatoil ASA, Martin Linges vei 33, 1364 Fornebu, Norway

Abstract

The relief of the South Atlantic is characterised by elevated passive continental margins along southern Africa and eastern Brazil, and by the bathymetric asymmetry of the southern oceanic basin where the western flank is much deeper than the eastern flank. We investigate the origin of these topographic features in the present and over time since the Jurassic with a model of global mantle flow and lithospheric deformation. The model progressively assimilates plate kinematics, plate boundaries and lithospheric age derived from global tectonic reconstructions with deforming plates, and predicts the evolution of mantle temperature, continental crustal thickness, long-wavelength dynamic topography, and isostatic topography. Mantle viscosity and the kinematics of the opening of the South Atlantic are adjustable parameters in thirteen model cases. Model predictions are compared to observables both for the present-day and in the past. Present-day predictions are compared to topography, mantle tomography, and an estimate of residual topography. Predictions for the past are compared to tectonic subsidence from backstripped borehole data along the South American passive margin, and to dynamic uplift as constrained by thermochronology in southern Africa. Comparison between model predictions and observations suggests that the first-order features of the topography of the South Atlantic are due to long-wavelength dynamic topography, rather than to asthenospheric processes. The uplift of southern Africa is best reproduced with a lower mantle that is at least 40 times more viscous than the upper mantle.

Keywords: South Atlantic, dynamic topography, topography, tectonic reconstructions, mantle flow, rifting

1. Introduction

The South Atlantic Ocean exhibits asymmetric bathymetry and topography. The bathymetric asymmetry (Hayes, 1988; Marty and Cazenave, 1989) is particularly pronounced in the southern South Atlantic (Morgan and Smith, 1992), with the deep Argentine Basin on the western flank (*e.g.* Shephard et al., 2012) and a shallow eastern flank, continuous with the anomalously elevated African Plateau (Nyblade and Robinson, 1994). Continental crust is ~ 30 km thick in the hinterland of both conjugate margins, yet it is covered by ~ 1.5 km of post-rift sediments on the South American side while being eroded on the African side (Blaich

et al., 2009). The topographic asymmetry of the South Atlantic is characterised by the southern African and Brazilian plateaus in the hinterland of two segments of elevated passive continental margin (*e.g.* Japsen et al., 2011).

Several models have been proposed to explain the observed bathymetric asymmetry of the South Atlantic Ocean that constitutes a deviation from the relationship between depth and age of ocean floor (*e.g.* McKenzie, 1967). Morgan and Smith (1992) proposed that asthenospheric flow could explain the flattening of old ocean floor, and attributed the asymmetry to differences in asthenospheric flow due to the asymmetric migration rates of the South American and African plates with respect to the deep mantle. In contrast, Doglioni et al. (2003) proposed that a general westward motion of the lithosphere with respect to the mantle results in an eastward flow of the asthenosphere, such that the eastern rift flank could be underlain by depleted, lighter

*Corresponding author. Tel.: +61 (0)2 9351 7576; fax: +61 (0)2 9351 2442

Email address: nicolas.flament@sydney.edu.au (Nicolas Flament)

asthenosphere, resulting in shallower bathymetry. Although quite different, these models both propose a shallow mantle origin for the topographic asymmetry of the South Atlantic; they are also exclusively inspired by and compared to present-day observations. Neither of these models address the elevated passive continental margins in South Africa and in Brazil nor the evolution of the region.

Here, we investigate the effect of mantle convection on the evolution of the topography of the South Atlantic. We introduce Earth deformation models that consider both mantle flow and lithospheric deformation. These models are forward in time and progressively assimilate space- and time-dependent boundary conditions derived from global tectonic reconstructions with continuously closing and deforming plates. They predict the evolution of mantle temperature, thickness of the continental crust, dynamic topography and isostatic topography. This global approach makes it possible to investigate the consequences of a given tectonic reconstruction for the dynamic evolution of a passive margin at continental scale and over tens of millions of year, including the post-rift phase. We implement two alternative kinematic models for the opening of the South Atlantic Ocean (Torsvik et al., 2009; Heine et al., 2013) and compare the predicted crustal thickness for South America, where results are most contrasted, to continent-scale Moho maps (Lloyd et al., 2010; Assumpção et al., 2013; Chulick et al., 2013). The models are also compared to present-day topography and bathymetry, and to an estimate of residual topography (Winterbourne et al., 2009) for the Atlantic. Furthermore, the predicted subsidence history is quantitatively compared to borehole tectonic subsidence, while the uplift history of southern Africa is qualitatively compared to the unroofing history constrained by thermochronology (Flowers and Schoene, 2010; Zhang et al., 2012).

2. A numerical model of mantle flow and lithospheric deformation

We introduce a new generation of forward models of mantle flow and lithospheric deformation with progressive data assimilation. We first present the equations solved for mantle convection and shearing of the lithosphere, and then describe the methods we use to obtain compositionally-distinct continents in global mantle flow models, and to implement deforming areas in global plate reconstructions.

2.1. Governing equations

We solve the finite-element problem of thermochemical convection within the Earth's mantle under the Boussinesq approximation (*e.g.* Spiegel and Veronis, 1960) using *CitcomS* (*e.g.* Zhong et al., 2008) modified to allow assimilation of data derived from global plate reconstructions.

The conservation of mass is expressed as

$$\nabla \cdot \mathbf{u} = 0 \quad (1)$$

where \mathbf{u} is the velocity. The conservation of momentum is expressed as

$$\begin{aligned} & -\nabla p + \nabla \cdot \left[\eta (\nabla \mathbf{u} + \nabla^\top \mathbf{u}) \right] \\ & = (-\alpha T + \delta\rho_{ch} C + \delta\rho_{ph} \Gamma) Ra \bar{g} \hat{\mathbf{r}} \end{aligned} \quad (2)$$

where p is the dynamic pressure, η the mantle viscosity, \top the transpose, α the coefficient of thermal expansivity, T the temperature, $\delta\rho_{ch}$ the chemical density, C the composition, $\delta\rho_{ph}$ the density difference across a phase change, \bar{g} a depth-dependent, non-dimensional acceleration of the gravity field, $\hat{\mathbf{r}}$ the radial unit vector and Ra is the Rayleigh number defined below. $\delta\rho_{ch}$ is non-dimensionalised and described in terms of the buoyancy ratio

$$B = \delta\rho_{ch} / \alpha_0 \rho_0 \Delta T \quad (3)$$

with ρ_0 the density and ΔT the superadiabatic temperature change across the mantle. Parameters are listed in Table 1. The phase function (*e.g.* Richter, 1973) is

$$\Gamma = 1/2 \left[1 + \tanh \left(\frac{\rho \bar{g} (1 - r - d_{ph}) - \gamma_{ph} (T - T_{ph})}{\rho g w_{ph}} \right) \right] \quad (4)$$

where r is the depth, d_{ph} and T_{ph} are the ambient depth and temperature of a phase change, γ_{ph} is the Clapeyron slope of a phase change, and w_{ph} is the width of the phase transition. In order to investigate the effect on dynamic topography of a phase change at $d_{ph} = 670$ km (case TC6, Table 2), we use $\delta\rho_{ph} = 7\%$ and $\gamma_{ph} = -2$ MPa K⁻¹ (Billen, 2008), $w_{ph} = 40$ km and $T_{ph} = 1667$ K.

The Rayleigh number Ra is defined by

$$Ra = \frac{\alpha_0 \rho_0 g_0 \Delta T h_M^3}{\kappa_0 \eta_0} \quad (5)$$

where h_M is the thickness of the mantle, η_0 the reference viscosity, and κ_0 the thermal diffusivity.

The conservation of energy is

$$c_p \frac{\partial T}{\partial t} = -c_p \mathbf{u} \cdot \nabla T + \nabla \cdot (c_p \kappa \nabla T) \quad (6)$$

where c_p is the heat capacity and t is time. The equation for advection of the composition field is

$$\frac{\partial C}{\partial t} + (\mathbf{u} \cdot \nabla) C = 0. \quad (7)$$

The composition field, C , is represented by tracers that are advected using a predictor-corrector scheme (McNamara and Zhong, 2004). The composition field is determined using the ratio method (Tackley and King, 2003), modified to give $C = 0$ if an element contains no tracers. This modification allows us to considerably limit the total number of tracers required to track compositionally distinct material in the uppermost and lowermost mantle.

Eqs. 1-7 are routinely used to solve the problem of thermochemical mantle convection in a viscous shell. They can also be used to solve for heat advection and diffusion upon stretching of the lithosphere (*e.g.* McKenzie, 1978; Jarvis and McKenzie, 1980), allowing us to solve both problems simultaneously given sufficient numerical resolution.

2.2. Data assimilation

Resolving the fully-dynamic, time-dependent problem of thermochemical mantle convection requires a resolution of the order of a kilometre to capture the physics of plate boundaries, including dislocation creep and yielding (*e.g.* Stadler et al., 2010). Because time-dependent, global models with such resolutions are still prohibitively expensive, we instead progressively assimilate boundary conditions derived in million year (Myr) increments from global tectonic reconstructions modified from Seton et al. (2012). These reconstructions use a hybrid absolute reference frame, based on a moving hotspot model (O'Neill et al., 2005) for the last 100 Ma, and a true-polar wander corrected paleomagnetic model (Steinberger and Torsvik, 2008) before 100 Ma.

Surface velocities are extracted from global reconstructions with continuously closing plates (Gurnis et al., 2012) and imposed as boundary condition in the mantle flow models (Fig. 1A). These velocities are exported using *GPlates* (Boyden et al., 2011) and then linearly interpolated for periods less than 1 Myr. We use a half-space cooling model to build a global thermal field of the lithosphere for each plate reconstruction that we test. In addition to the age of the ocean lithosphere implied by the tectonic reconstruction, we use the tectonothermal age of the continental lithosphere

(Artemieva, 2006) simplified to three age bins (Fig. 1A). This global thermal structure of the lithosphere, assimilated to a depth of 64 km, is merged with the dynamically evolving temperature field (see Matthews et al., 2011, for more details), except in areas that have undergone kinematically-imposed plate deformation (see below). This progressive assimilation of the thermal lithosphere (Fig. 1B) allows us to limit the development of Rayleigh-Taylor instabilities, and to control the surface heat flux as well as the topography of rigid plates.

Finally, in order for our viscous simulations to capture subduction asymmetry and trench roll-back and other aspects of subduction zones, we build a global model of the shallow thermal structure of slabs based on the location and polarity of subduction zones in the reconstructions. The shallow thermal structure of slabs (to 350 km depth) dipping 45° in the mantle, derived from the age of the subducting oceanic lithosphere, is merged with the dynamically evolving temperature field at each time step (see Bower et al., 2013, for more detail). In addition, we ensure that subducting slabs appearing during the modelled period are progressively inserted into the upper mantle, using the age of appearance and the convergence defined for each subduction zone. The slab assimilation attempts to minimise the difference between the slab buoyancy flux in the upper mantle and that predicted by the plate reconstruction.

2.3. Model setup and initial condition

We solve the convection problem for the full shell divided into 12 caps, each consisting of $128 \times 128 \times 64$ elements for a total of $\sim 13 \times 10^6$ nodes. The average lateral resolution is ~ 50 km at the surface and ~ 28 km at the core-mantle boundary (CMB), and the average radial resolution is ~ 45 km. Radial mesh refinement is used to increase the resolution to ~ 15 km in the top boundary layer, ~ 27 km in the bottom boundary layer, while keeping a minimum resolution of ~ 100 km in the mid-mantle.

The viscosity depends on pressure and temperature as

$$\eta = \eta_0(r) (1 + \eta_C C) \exp\left(\frac{E_\eta}{T^* + T_\eta} - \frac{E_\eta}{T_b + T_\eta}\right) \quad (8)$$

where $\eta_0(r)$ is a pre-factor defined for five layers: upper mantle (UM) above 160 km, UM between 160-310 km, UM between 310-410 km, UM below 410 km, and lower mantle (Table 2 and Fig. 2). $\eta_0(r)$ linearly increases with depth in the lower mantle for cases TC7, TC8 and TC9 (Table 2). η_C is the intrinsic compositional viscosity pre-factor used for the chemically dis-

tinct continents but not for the chemically distinct lowermost mantle; E_η is the non-dimensional activation energy, $T^* = \min(\max(T, 0), 1)$, T_b is the background temperature of the mantle and T_η is an ‘‘activation’’ temperature. We test different radial viscosity structures of the upper mantle, transition zone and lower mantle (Table 2 and Fig. 2). All cases were run using 96 processors, requiring $\sim 30,000$ core-hours on the Sun Constellation VAYU of the Australian National Computational Infrastructure (NCI).

The initial condition, at 200 Ma, consists of a global temperature field ($T_b = 0.5$) with cold slabs inserted to a given depth (Fig. 1C and Table 2), and a cold surface thermal boundary layer (Fig. 1B-C) as described in Section 2.2. For subduction zones thought to have initiated less than ~ 50 million years before 200 Ma, slabs are inserted to shallower depths assuming a sinking rate of 5 cm yr^{-1} in the upper mantle and 1.2 cm yr^{-1} in the lower mantle (van der Meer et al., 2009). We apply a kinematic and isothermal ($T_s = 273 \text{ K}$) boundary condition at the top surface, and a free-slip and isothermal boundary condition at the CMB. Initial tests with $T_{\text{cmb}} = 3098 \text{ K}$ led to mantle plumes arising in areas of passive mantle upwelling. Although loosely consistent with geological observations, these mantle plumes did not exactly match observed hotspot tracks nor the location of large igneous provinces. In order to limit the occurrence of such plumes that modify the long-wavelength dynamic topography, we either (i) decrease T_{cmb} to 2185 K in ‘‘cold’’ cases (labeled xCx in Table 2) with a minimum temperature drop of 500 K across the bottom thermal boundary layer (Lay et al., 2008), or (ii) decrease T_{cmb} to 2685 K in ‘‘hot’’ cases (labeled xHx in Table 2) that include an initially laterally uniform 113-km-thick layer of compositionally denser material at the base of the mantle ($\sim 2\%$ of the Earth’s mantle, see Hernlund and Houser 2008, Tables 1 and 2) throughout which the temperature decreases to the background value following a half-space cooling model.

2.4. Global tectonic reconstructions with deforming plates

We introduce global tectonic reconstructions that account for deformation at plate boundary zones, focusing on the passive margins of the South Atlantic Ocean and the Andes. Deformation is obtained by building on the continuously closed plates formulated in *GPlates* (Gurnis et al., 2012). Deforming areas are restricted to defined boundaries in time and space, and the deformation and velocity field is interpolated between control points. This method is to be fully described in a forthcoming paper (Gurnis et al., 2013).

We implement two recently proposed kinematic models for the opening of the South Atlantic (Torsvik et al., 2009, cases labeled Txx, and Heine et al., 2013, cases labeled Hxx). The seafloor spreading history is largely the same in both scenarios. They mostly differ in the timing of rifting in the central and south segments (between 131-112 Ma in the reconstruction of Torsvik et al. (2009), see Fig. 3A-C, and between 145-115 Ma in that of Heine et al. (2013), see Fig. 3D-F). The kinematics of deformation within southern South America also differ in these scenarios, with highly oblique extension in the reconstruction of Torsvik et al. (2009) (Fig. 3A-C) but deformation distributed around rigid blocks over a large area in the reconstruction of Heine et al. (2013) (Fig. 3D-F). To implement deformation along conjugate passive margins, we first define the landward and seaward limits of extended continental crust. We refine the continent-ocean boundary (COB) proposed by Torsvik et al. (2009) based on the identification of *bona fide* oceanic crust on seismic lines by Winterbourne et al. (2009, Supplementary Figs. 1 and 2). We define the landward limit of extended crust to lie along the landward edge of large horizontal gradients within the upward continued Bouguer gravity anomaly (related to regional changes in crustal thickness, Supplementary Fig. 1), and outboard of outcropping Paleozoic and Precambrian geological units (Bouysson and Palfreyman, 2000, Supplementary Fig. 2). The magnitude and direction of deformation within these regions is a function of the relative motion of the rigid plates either side, and assume a constant ratio of the widths of the conjugate margins along small circles for the given Euler pole (see Supplementary Section 1 for more detail). While simplified from the complex margins of the South Atlantic (*e.g.* Unternehr et al., 2010), this assumption of uniform stretching of the lithosphere is appropriate for the resolution and the physics of our large-scale geodynamic model. Deformation within Africa and southern South America is described by defining deforming regions bounded by rigid blocks, and linearly interpolating the surface velocities within the deforming regions from these bounding constraints.

Deformation is also implemented in the central Andes between 45-0 Ma, following the reconstruction of Arriagada et al. (2008, see Supplementary Section 1). Although this deformation significantly postdates the South Atlantic breakup, its implementation shifts the central Andean margin by 500 km to the west prior to 45 Ma, thereby influencing the evolution of mantle structure and dynamic topography.

For each of the two South Atlantic reconstructions, we develop a global reconstruction with continuously

closing plates back to 200 Ma, and a set of input files for the geodynamic models. The deformation is assimilated into the geodynamic model via the velocity field (Fig. 3G-H). While the velocity field is constant in rigid South America, the smooth gradient in the deforming passive margins imposes shearing of the continental lithosphere in the geodynamic model (Fig. 3G-H).

2.5. Continental topography in global mantle flow models

2.5.1. Modelling continents

We model continental isostasy based on the assumption that an isopycnic depth exists at which thermal and chemical buoyancies are compensated (Jordan, 1975). We consider three continental columns based on tectonothermal age (Artemieva, 2006). Because the thickness of the continental lithosphere is unknown in the past, each lithospheric column is assumed to be initially laterally homogeneous, consisting of 40-km-thick continental crust underlain by continental thermochemical lithosphere of thickness 250 km (Archean), 165 km (Proterozoic) and 135 km (Phanerozoic), as suggested by global estimates (Artemieva, 2009). The continental crust and three different types of continental lithosphere are modelled using tracers of distinct buoyancies (Eq. 3 and Table 1) that are defined in the initial condition (Fig. 1D-E) and advected throughout the domain. The average number of tracers per element is 30. We include “ambient” tracers (representing background mantle composition) to 410 km depth to ensure a smooth numerical transition from distinct tracers to ambient tracers to no tracers. Likewise, we include a 150-km-thick layer of ambient tracers above the basal boundary layer in the initial condition of the cases representing a dense layer (HH1, HH2 and HH3, Table 2). The lithospheric temperature field is assimilated in rigid continental areas throughout the model run, but not in deforming areas from the onset of deformation onwards, in order to capture changes in topography associated with the thermal equilibration of the lithosphere.

Because the initial topography is poorly known, we scale the buoyancy of the different continental tracers in order to obtain initially flat continents (Fig. 1F) with Precambrian areas ~ 3.5 km above ocean floor younger than 2.5 Ma, as observed globally (*e.g.* ETOPO1, Amante and Eakins, 2009).

2.5.2. Computation of topography

We compute two types of topography: “total model topography” and dynamic topography. The “total model

topography” is obtained by re-solving the Stokes equation (*e.g.* Eq. 2) every 10 Myr but with a no-slip surface boundary condition to avoid the surface traction imposed by plate velocities that would result in a large-amplitude signal interfering with the dynamic topography. This “total model topography” includes the effects of isostasy, mantle flow and thermal diffusion in the thermal boundary layer. Surface dynamic topography is computed in the same way, except with just the density from the thermal and composition fields below 350 km depth. Both topographies are obtained by scaling the radial stress σ'_{rr} on the top model surface following

$$h = \frac{\eta_0 \kappa}{\Delta\rho g_0 R_0^2} \sigma'_{rr}, \quad (9)$$

where all variables are defined in section 2.1 and Table 1, except R_0 the radius of the Earth and $\Delta\rho$, which is the density difference between the shallow mantle $\rho_{sm} = 3340 \text{ kg m}^{-3}$ and either air $\rho_a = 0$ or seawater $\rho_w = 1030 \text{ kg m}^{-3}$. We load the total model topography with water (Fig. 6D-F) by distributing a constant ocean volume of $1.36 \times 10^{18} \text{ m}^3$ onto low lying areas, resulting in air-loaded continents and water-loaded oceans. For dynamic topography, air-loaded results are presented in Fig. 6A-C to preserve smooth gradients. In other figures, dynamic topography results are water-loaded in the oceans (Figs. 7 and 8A-D) and air-loaded in the continents (Fig. 8E).

Computed continental elevations are lower than observed ones (Precambrian areas ~ 3.5 km above ocean floor younger than 2.5 Ma), because the assimilation depth for the temperature structure of the lithosphere (64 km) is much smaller than the keels of the Archean provinces (250 km). We used two strategies to increase continental elevations: (i) adding to the results a chemical elevation correction $h_c = B \alpha \Delta T \Delta H_c$ and a thermal elevation correction $h_t = -0.539 \alpha T_m \Delta H_t$, where ΔH_c and ΔH_t are, respectively, the deviations between calculated and target thickness of the thermal and chemical lithosphere for Archean continents; (ii) restarting cases TC1 and HH1 at the beginning of deformation (150 Ma) with continental tracers conforming to the boundaries and thickness of the tectonic provinces, and an increased buoyancy of the continental crust (cases TC1R and HH1R, see Table 2).

3. Contributions of mantle flow and lithospheric deformation to the evolution of the topography

Here we present the main results of our model: predicted temperature, thickness of continental crust, dynamic topography and model topography.

3.1. Present-day temperature field

To assess the thermal state of the model, we analyse the evolution of average CMB heat flux. Average CMB heat flux reaches equilibrium by 150 Ma for case HH2, while appearing to oscillate with a period $\gtrsim 160$ Myr and within $\lesssim 15\%$ of equilibrium for other cases (see Supplementary Fig. 3 and Supplementary Section 2.1). These long period, low-amplitude oscillations in CMB heat flux are deemed acceptable in the context of comparing cold, transient anomalies in the predicted present-day temperature field (Fig. 4A) to a *S*-wave tomography model (Grand, 2002) for a cross-section taken along a South Atlantic flowline at 45°S (Fig. 4B-C). We limit this comparison to cases with the most contrasting viscosity structures. This cross-section of the temperature field shows that the assimilation of shallow thermal structure of slabs results in asymmetric subduction, and in slabs that continuously extend to mid-mantle depths under South America. Model slabs are broadly similar across all cases, with the exception of case TC5 that has much larger volumes of cold mantle. Slabs have sunk deeper for cases with smaller lower mantle viscosities (notably cases TC8, TC9 and HC2), as expected and reflected by the difference in the viscosity structure for cases HH1 (Fig. 4C) and TC8 (Fig. 4D).

3.2. Evolution of continental crustal thickness

We compute the crustal thickness defined as the depth to the deepest element containing at least two tracers of crustal composition. Given the radial resolution of ~ 15 km in the uppermost part of our model, results are limited to six depth bins between 0 and 82.5 km.

The evolution of the thickness of the continental crust for cases TC1 and HH1 (Fig. 5) reflects the different timing of the opening of the South Atlantic between the two reconstructions, with thinning of the continental crust starting earlier in case HH1. The more distributed deformation in case HH1 also results in smoother gradients in crustal thickness in southern South America and in northern Africa (Fig. 5C-F).

The benefit of prescribing deformation is clear from the extended continental crust offshore southern Argentina (to the east of well 14/05-1A, orange star on Figs. 6C and F) for which the continental crust is thin as expected for case HH1 (with prescribed deformation) but not for case TC1 (without). Some smearing of the compositional field is also observed north and south of the prescribed South Atlantic deforming passive margins (Fig. 5C-F). Crustal thickening occurs at convergent margins in the model (Fig. 5A-B-D-E), and tracers are excluded within 350 km of subduction zones to limit

this effect. As a result, the implemented Andean deformation scenario (Arriagada et al., 2008) only gives significant crustal thickening in the central part of the Andes (Fig. 5C-F).

3.3. Evolution of topography

The model predicts the evolution of dynamic topography as well as isostatic topography in the continents, which is particularly relevant in deforming areas. The evolution of the minimum dynamic topography shows that following an initial transient phase from the initial condition at 200 Ma, all models reach equilibrium between 150-140 Ma (Supplementary Fig. 4 and Supplementary section 2.2). Fig. 6A-C and Fig. 6D-F respectively show the evolution of air-loaded dynamic topography and total model topography for case HH1R since the beginning of modelled South Atlantic deformation (150 Ma).

3.3.1. Evolution of dynamic topography

As expected, the pattern of dynamic topography at 150 Ma (Fig. 6A-C) is characterised by narrow strips of negative dynamic topography > -1200 m along the western Americas and southern Eurasia, and a broad kidney-shaped positive dynamic topography < 1000 m centred on central Africa. The dynamic topography highs are broader than the dynamic topography lows that correspond to passive return flow in this subduction-driven model. The variation in amplitude along subduction zones reflects the dependence of slab buoyancy on the age of the subducting lithosphere. The pattern and amplitude at 150 Ma (see Supplementary Animation) persists to present-day, although the dynamic topography lows broaden. In particular, the dynamic topography low along western South America widens from ~ 70 Ma (see Supplementary Animation) as the trench rolls back and the continent overrides subducting material, as noted in previous studies (Shephard et al., 2010; Husson et al., 2012). At present, only eastern Brazil remains on the edge of the dynamic topography high centred to the west of southernmost Africa. The location of this dynamic topography high and the present-day east-west gradient in dynamic topography across northern South America are consistent with multiple estimates of residual topography, and dynamic topography models (Flament et al., 2013, and references therein), although patterns and amplitudes vary between estimates. The active Afar and East African upwellings that appear in estimates of residual topography (*e.g.* Flament et al., 2013, and references therein) and in instantaneous (Lithgow-Bertelloni and Silver, 1998; Gurnis et al., 2000) and backward advected models based

on tomography (Conrad and Gurnis, 2003; Moucha and Forte, 2011) are not predicted by subduction-driven forward models (*e.g.* Ricard et al., 1993, and this study).

3.3.2. Evolution of total model topography

The total topography initially consists of isostatically flat continents standing ~ 3500 m above ocean floor younger than 2.5 Ma (Figs. 1F and 6F). In the oceans, the bathymetry deepens away from spreading centres, reflecting the assimilated thermal structure of the lithosphere (Fig. 6D-F). The long-wavelength dynamic topography results in a tilt of South America to the west (Fig. 6D and E). As expected, rifted areas show rapid initial subsidence (Fig. 6D and E) followed by protracted thermal subsidence until the present-day (Fig. 6F). The predicted present-day total topography (Fig. 6F) mirrors crustal thickness (Fig. 5F) with high elevations (thick crust) in the central Andes and low elevations (thin crust) along the passive margins and great African rifts. In addition, two broad low-lying areas are predicted in northwestern South America and in northeastern Africa, and two broad elevated areas are predicted in southern Africa and eastern Brazil. This broader topography reflects the present-day dynamic topography pattern (Fig. 6C).

4. Comparison of model predictions to geological and geophysical data

4.1. Comparison to mantle tomography

The predicted present-day temperature field (Fig. 4) can be compared to mantle tomography models that are not used as input. A fully quantitative comparison of model prediction to a mantle tomography model (Schuberth et al., 2009) is beyond the scope of this topography-focused study. Instead, we carry out a qualitative comparison by overlying the contours of mantle 10% colder than ambient for selected cases on the *S*-wave mantle tomography model of Grand (2002, Fig. 4B). Our model slabs match the most pronounced high-velocity seismic anomalies in the upper half of the mantle along the flowline on Fig. 4B. A similar conclusion can be drawn from the three alternative tomography models shown in Supplementary Fig. 5, although high-velocity anomalies extend deeper under Africa in these models. Model slabs are also broadly compatible with the structure of the lowermost mantle, as they do not lie over the main low seismic velocity anomaly centred on 20°E (except for cases TC5 and TC9). A similar conclusion can be drawn from Supplementary Fig. 5 that also shows that the longitudinal position and thickness of the

African Large Low Shear Velocity Province (LLSVP) varies between tomography models. In addition, the dense and hot layer included in cases HH1, HH2 and HH3 limits the lateral spreading of lower-temperature mantle at the core mantle boundary (Fig. 4B). The thickness of this dense layer has quadrupled from 113 km to ~ 500 km (dashed white contour in Fig. 4C) at a location that is broadly consistent with that of the African LLSVP, confirming that subducting slabs influence the location of LLSVPs (Bower et al., 2013). The small final thickness of the model LLSVP (~ 500 km compared to > 1500 km in the tomography, Fig. 4C) is likely due to the short integration time (200 Myr) and to relatively large density anomaly of the basal layer (+ 3.6% or $B = 0.5$, Table 1). Hot mantle has also accumulated over a thickness of ~ 1000 km at a location consistent with the location of the African LLSVP (Fig. 4D) for case TC8 in which the lower mantle is isochemical with depth-dependent viscosity (Fig. 4D).

4.2. Comparison to continental-scale crustal thickness maps

Continental-scale crustal thickness maps (Lloyd et al., 2010; Assumpção et al., 2013; Chulick et al., 2013) do not show the deep troughs predicted in southern South America for the cases based on our implementation of the reconstruction of Torsvik et al. (2009, Fig. 5C). Such sharp features should be captured given the resolution of Moho maps for South America (Lloyd et al., 2010), despite the uneven seismic coverage across the continent. This result suggests that reconstructions implying distributed deformation in southern South America (*e.g.* Heine et al., 2013) are more appropriate to model the kinematics of the opening of the South Atlantic. Since the choice of reconstruction does not influence large-scale mantle flow and dynamic topography, the difference between the prediction for each reconstruction could have been estimated by a stand-alone analysis of the finite strain they predict.

4.3. Comparison to present-day residual topography and topography

4.3.1. Comparison between predicted dynamic topography and present-day residual topography

We compare the predicted present-day, water-loaded dynamic topography to the residual topography estimated by Winterbourne et al. (2009, Fig. 10) along the Atlantic margins and mid-oceanic ridge (Fig. 7A-C) and to four independent computations of dynamic topography (Ricard et al., 1993; Steinberger, 2007; Conrad and

Husson, 2009; Spasojevic and Gurnis, 2012). Comparison between this residual topography and dynamic topography is not straightforward in the absence of a reference level in the calibration between gravity and residual topography (admittance) proposed by Winterbourne et al. (2009), and because of the dependence of dynamic topography amplitude on the boundary conditions (Thoraval and Richards, 1997) and depth for which it is calculated. For instance, calculating dynamic topography for a free-slip, rather than a no-slip surface decreases the predicted amplitude (dashed black line for case TC1 in Fig. 7A-C), and resulting in less pronounced gradients. Predicted trends and amplitudes are similar across all modelled cases, and gradients are most pronounced for cases TC4, TC5, TC8 and TC9 (Supplementary Fig. 6).

The fit between residual topography and dynamic topography is overall relatively poor for the five models considered. The residual topography presents higher-frequency variations than instantaneous models based on tomography (Steinberger, 2007; Conrad and Husson, 2009; Spasojevic and Gurnis, 2012) and in turn than time-dependent forward models (this study; Ricard et al., 1993). As expected, results for case TC1 with free-slip boundary conditions are most similar to the results of Ricard et al. (1993). Trends in residual topography along the American margin are broadly reproduced by all models (Fig. 7A), but estimates along South America tend to be too large for forward models, and too negative for the model of Steinberger (2007). The prediction of instantaneous models compare better to residual topography along the mid-Atlantic ridge and the African margin, especially in the south where the dynamic topography predicted by forward models exceeds the estimated residual topography (Fig. 7B-C). Overall, the dynamic topography predicted by the models of Conrad and Husson (2009) and Spasojevic and Gurnis (2012), both based on *S*-wave tomography model S20RTS (Ritsema et al., 1999) present the least deviation to the estimated residual topography, but they also present the smallest variations in amplitude and do not capture shorter wavelength variations in residual topography. The model of Steinberger (2007), based on a weighted average of *S*-wave tomography models, captures some of these shorter wavelength variations (at $\sim 40^\circ\text{N}$, Fig. 7A, and at $\sim 5^\circ\text{N}$, Fig. 7C), but it significantly deviates from the estimated residual topography along the South American passive margin, between $\sim 15\text{-}30^\circ\text{N}$ along the Atlantic ridge (Fig. 7B) and between $\sim 10\text{-}20^\circ\text{S}$ along the African passive margin (Fig. 7C).

We suggest that including active upwellings in future forward models would change the distribution of

dynamic topography highs and reduce the offset in amplitude between dynamic topography predicted by such models and positive residual topography. In addition, the buoyancy of the passive thermal upwelling below southern Africa could be partially offset by compositionally denser material, extending from the core-mantle boundary to ~ 1200 km depth in the lower mantle (Simmons et al., 2007). In principle, an inversion could be carried out to find a set of boundary conditions and mantle viscosity structure that reproduces the residual topography estimated by Winterbourne et al. (2009). This inversion would be best suited for instantaneous mantle flow models, and it would still be limited by the absence of a reference level for the admittance. Contrary to the model presented herein, such instantaneous models could not be used to investigate mantle flow, let alone lithospheric stretching, as far back as the Cretaceous.

4.3.2. Comparison between predicted total model topography and present-day topography

We next compare the present-day total model elevation predicted by our model to the one arc minute global relief model ETOPO1 (Amante and Eakins, 2009). In the ocean, we plot the filtered bathymetry along a flow-line at 45°S . The shallowest part of the ridge is set as datum for both the model and the observation. Modelled and observed bathymetry both display a marked asymmetry (Fig. 7D) with the eastern flank of the ocean ~ 1000 m shallower than the western flank. Since the bathymetry associated with the cooling of the lithosphere is assimilated via a half-space cooling model, the asymmetry is primarily controlled by dynamic topography. The model bathymetry is steeper than observed (Fig. 7D), which could be due to model vertical resolution (15 km in the lithosphere). We nevertheless attribute the South Atlantic bathymetric asymmetry to the whole mantle process of long-wavelength, subduction-driven dynamic topography (Fig. 6C), in contrast to previous asthenospheric models (Morgan and Smith, 1992; Doglioni et al., 2003). In this respect, it is worth noting that the asymmetry predicted for case HH3 is less pronounced than that predicted by case HH2 that is identical except for a low-viscosity asthenosphere. Indeed, a low-viscosity asthenosphere leads to reduced amplitude of dynamic topography (Supplementary Fig. 6). The anomalous depth of the Argentine Basin has previously been attributed to mantle flow (Shephard et al., 2012).

On the continents, the location of predicted broad elevated areas (Fig. 6F) matches the location of the southern African and Brazilian plateaus (dashed black outlines in Fig. 6F): our model also predicts the two seg-

ments of elevated passive continental margins observed in the South Atlantic (Japsen et al., 2011). To quantitatively estimate how well these two elevated passive continental margins are predicted, we compare the predicted and observed difference in elevation between the Kaapvaal (yellow outline in Fig. 6F) and São Francisco (green outline in Fig. 6F) cratons in Table 2. Both of these cratons, in the hinterland of the elevated continental margins, present relatively large mean elevations (~ 1020 m for the Kaapvaal Craton and ~ 610 m for the São Francisco Craton). Keeping in mind that both observed and modelled topographies are noisy, the Kaapvaal Craton is predicted to be more elevated than the São Francisco Craton in all cases (Table 2). The difference in elevation predicted by the model is larger than observed, which again suggests that the lower mantle could be chemically denser than average under Africa. Indeed, the elevation difference predicted by cases HH1 and HH2, that include chemically dense material in the lowermost mantle, is closer to the observation. The predicted elevation difference also decreases with the viscosity of the lower mantle, and when a phase change is considered (Table 2).

4.4. Comparison to geological proxies of tectonic subsidence and rock uplift

We compare modelled topography to tectonic subsidence in subsided areas (South American passive margin, Fig. 6A-C) and to thermochronology results in uplifted areas (southern African plateau, Fig. 6A-C).

4.4.1. Comparison to tectonic subsidence

The total predicted model topography is directly compared to borehole data from four wells on the South American passive margin that were not used in reconstructing the deforming plates (Supplementary Section 1) and are therefore fully independent. Wells in the Bahia Sul, Espirito Santo, and Santos basins were backstripped by Chang et al. (1992) assuming local isostasy, constant sea level, constant paleobathymetry, and extrapolating the stratigraphic record to basement based on seismic reflection information (the first segment of the tectonic subsidence is shown as a dashed line in Fig. 8A-D). In the North Falkland Basin, we compare our results to the tectonic subsidence of well 14/05-1A backstripped by Jones et al. (2004).

The uncertainty associated with paleobathymetry is small for well 14/05-1A, except between ~ 95 - 85 Ma when it reaches ~ 100 m (Jones et al., 2004). Tectonic subsidence can at best be determined within a few tens of meters because variability in lithology and associated

porosity result in decompaction uncertainties. There are also uncertainties associated with the biostratigraphic ages, so that the age is usually determined within a few million years, although it is ± 10 Myr for the early section of well 14/05-1A (Jones et al., 2004).

Given these uncertainties and the resolution of our global model, the agreement between water-loaded total model topography and tectonic subsidence (Fig. 8A-D) is good. First, the model captures the dynamics of rifting expected for pure shear of the lithosphere (McKenzie, 1978): initial rapid tectonic subsidence during the rifting phase followed by a protracted phase of tectonic subsidence associated with thermal thickening of the lithosphere. The amplitude (timing) of both the rifting phase and the thermal subsidence phase are predicted (reproduced) within a few tens of meters (within a few million years), *i.e.* within error. The relatively poorer fit of the timing of rifting for the well in the Espirito Santo Basin suggests that either the assumptions of constant paleobathymetry and seismic extrapolation to basement (Chang et al., 1992) and/or the plate reconstruction (Heine et al., 2013) should be adjusted for this basin. In comparison, results for case TC4 (Supplementary Fig. 7) suggest that stretching initiates too late along the whole margin in the reconstruction of Torsvik et al. (2009).

The dotted lines in Fig. 8A-D and Supplementary Fig. 7 show the difference between total model topography and dynamic topography. Even though the amplitude of isostatic topography (~ 4 - 5 km) is one order of magnitude larger than that of dynamic topography ($\lesssim 700$ m), the agreement between model and data is much better when dynamic topography is considered. This suggests that jointly modelling shear of the lithosphere and mantle flow may be appropriate to model the large scale lithospheric evolution of passive margins, despite the complexity of the structure of the thinned crust (*e.g.* Unternehr et al., 2010). In this respect, it is worth noting that even in the Basin and Range, for which the simple-shear stretching model was formulated (Wernicke, 1985), the lithosphere appears to extend symmetrically (Lekic et al., 2011).

The three wells in the east Brazil rift system show an acceleration of subsidence that starts earlier and is more pronounced in the north (< 900 m of subsidence since ~ 65 Ma) than in the south (~ 500 m of subsidence since ~ 50 Ma). The dynamic subsidence of ~ 400 - 700 m since 80 Ma predicted for these wells by case HC1 (grey lines in Fig. 8A-D) suggests that this acceleration of subsidence could be due to the evolution of dynamic topography. Similarly, the regional Late Cretaceous unconformity in the North Falkland Basin (Jones et al.,

2004, Fig. 8D) coincides with ~ 170 m of dynamic uplift predicted by case HC1 between 80 and 50 Ma. The agreement between model and data for the east Brazil and North Falkland wells since 80 Ma illustrates the contribution of mantle flow to tectonic subsidence.

4.4.2. Comparison to a thermochronology study

Our model predicts that southern Africa has been uplifting since the Cretaceous, consistent with the results of a recent forward mantle flow model (Zhang et al., 2012, hereafter referred to as ZZ12). The main differences between the model presented here and ZZ12 are the plate reconstructions (see Zhang et al., 2010), the total dimensional time (450 Ma in ZZ12 and 200 Myr here), the data assimilation (limited to plate velocities in ZZ12), and the resolution (~ 135 km laterally and ~ 60 km radially in ZZ12, ~ 50 km and ~ 45 km here).

As in Zhang et al. (2012), we qualitatively compare the trends in predicted dynamic topography to the burial and unroofing history of the eastern Kaapvaal Craton constrained by inverse modelling of (U-Th)/He thermochronometry (Flowers and Schoene, 2010, Fig. 8E). Model results for this study are averaged for the whole Kaapvaal Craton rather than sampled at a point location and are consistent with the unroofing of the eastern Kaapvaal Craton from ~ 110 Ma (Fig. 8E). The rapid unroofing of the Kaapvaal Craton is arguably better reproduced by the model here, predicting a main phase of dynamic uplift of ~ 400 m between ~ 120 -80 Ma, while ZZ12 predicts ~ 300 m of dynamic uplift between ~ 130 -85 Ma.

Both ZZ12 and our model predict one main period of uplift for southern Africa, suggesting that processes other than subduction-driven dynamic topography are required to explain a second period of accelerated erosion during the Eocene-Oligocene, deduced from apatite fission track studies (*e.g.* Moore et al., 2009). In our model, the dynamic uplift of southern Africa from ~ 130 Ma is due to its relative motion away from the Pacific plates subducting along the western South American margin (Seton et al., 2012, Fig. 6A-C). In contrast, southern South America has remained over a subduction zone throughout this period (Fig. 6A-C) and displays smaller variations in dynamic topography (Fig. 8D). Note that cases TC5, TC8 and TC9 are difficult to reconcile with the unroofing history as constrained from thermochronometry (Fig. 8E), emphasising the role of temperature-dependent viscosity, absent in TC5, and suggesting that the lower mantle needs to be at least 40 times more viscous than the upper mantle to satisfy this geological constraint. Although slightly larger than a previous estimate (lower mantle 10 times more viscous

than the upper mantle, Gurnis et al., 2000), this result is consistent with early work on the geoid (Ricard et al., 1993).

5. Conclusion

We developed a model of global mantle flow and lithospheric deformation to simultaneously investigate the evolution of post-Jurassic dynamic and isostatic topography. Comparing model predictions to both present-day and historical constraints provides insights on the processes that led to the topographic asymmetry of the South Atlantic Ocean, and loose constraints on the properties of the Earth's mantle. The model predicts the salient present-day asymmetry of the South Atlantic, both in the oceanic and continental domains, and model slabs are a good fit to high-velocity seismic anomalies in mantle tomography. The agreement between predicted dynamic topography and residual topography is not as good for time-dependent forward model than for instantaneous backward advocated mantle flow models. This could be improved, while preserving the fit to other observations, by including thick thermochemical LLSVPs and active upwellings in future forward mantle flow models. Model predictions are also compatible with local geological constraints on the evolution of the tectonic subsidence along the South American passive margin and uplift of the South African plateau, as long as the lower mantle is at least 40 times more viscous than the upper mantle. Larger-scale compilations of geological data on the Phanerozoic vertical motion of Africa and South America would further constrain mantle properties. We suggest that the topographic asymmetry of the South Atlantic could be due to a whole mantle process (long-wavelength dynamic topography) rather than to asthenospheric processes (Morgan and Smith, 1992; Doglioni et al., 2003), and we attribute part of the uplift of southern Africa to its motion away from the dynamic topography low along the South American subduction zone. This should be taken into account in future studies attempting to constrain the nature and the buoyancy of the African LLSVP from observations.

6. Acknowledgments

N.F. was supported by Statoil ASA, M.G. was partially supported by Statoil ASA and by the National Science Foundation under grants CMMI-1028978, EAR-1161046 and EAR-1247022, S.W. and R.D.M. were supported by Australian Research Council (ARC) grant FL0992245, M.S. was supported by ARC grant

DP0987713, and C.H. was supported by ARC grant LP0989312. Computer simulations were carried out on the Sun Constellation VAYU cluster of the Australian National Computational Infrastructure. Figs. 1, 4, 5, 6, 7 and 8A-D were prepared using the Generic Mapping Tools (Wessel and Smith, 1998). The original *CitcomS* software was obtained from CIG, Computational Infrastructure for Geodynamics (<http://geodynamics.org>). We thank L. Husson and an anonymous reviewer for their detailed and constructive comments.

References

- Amante, C., Eakins, B. W., 2009. ETOPO1 1 Arc-Minute Global Relief Model: Procedures, Data Sources and Analysis. NOAA Technical Memorandum NESDIS NGDC-24.
- Arriagada, C., Roperch, P., Mpodozis, C., Cobbold, P., 2008. Paleogene building of the Bolivian Orocline: Tectonic restoration of the central Andes in 2-D map view. *Tectonics* 27 (6), doi:10.1029/2008TC002269.
- Artemieva, I. M., 2006. Global 1×1 thermal model TC1 for the continental lithosphere: implications for lithosphere secular evolution. *Tectonophysics* 416 (1), 245–277, doi:10.1016/j.tecto.2005.11.022.
- Artemieva, I. M., 2009. The continental lithosphere: reconciling thermal, seismic, and petrologic data. *Lithos* 109 (1), 23–46, doi:10.1016/j.lithos.2008.09.015.
- Assumpção, M., Feng, M., Tassara, A., Julià, J., 2013. Models of crustal thickness for South America from seismic refraction, receiver functions and surface wave tomography. *Tectonophysics*, doi:10.1016/j.tecto.2012.11.014.
- Billen, M. I., 2008. Modeling the dynamics of subducting slabs. *Annu. Rev. Earth Planet. Sci.* 36, 325–356, 10.1146/annurev.earth.36.031207.124129.
- Blaich, O. A., Faleide, J. I., Tsikalas, F., Franke, D., León, E., 2009. Crustal-scale architecture and segmentation of the Argentine margin and its conjugate off South Africa. *Geophys. J. Int.* 178 (1), 85–105, doi:10.1111/j.1365-246X.2009.04171.x.
- Bouysson, P., Palfreyman, D., 2000. Geological Map of the World at 1:25 M. Commission for the Geological Map of the World.
- Bower, D. J., Gurnis, M., Seton, M., 2013. Lower mantle structure from paleogeographically constrained dynamic Earth models. *Geochem. Geophys. Geosy.* 14, doi:10.1029/2012GC004267.
- Boyden, J. A., Müller, R. D., Gurnis, M., Torsvik, T., Clark, J. A., Turner, M., Ivey-Law, H., Watson, R. J., Cannon, J., 2011. Next-generation plate-tectonic reconstructions using GPlates. *Geoinformatics: Cyberinfrastructure for the Solid Earth Sciences*, 95–114.
- Chang, H. K., Kowsmann, R. O., Figueiredo, A. M. F., Bender, A., 1992. Tectonics and stratigraphy of the East Brazil Rift system: an overview. *Tectonophysics* 213 (1), 97–138.
- Chulick, G. S., Detweiler, S., Mooney, W. D., 2013. Seismic structure of the crust and uppermost mantle of South America and surrounding oceanic basins. *J. S. Am. Earth Sci.* 360, 260–276, doi:10.1016/j.jsames.2012.06.002.
- Conrad, C. P., Gurnis, M., 2003. Seismic tomography, surface uplift, and the breakup of Gondwanaland: Integrating mantle convection backwards in time. *Geochem. Geophys. Geosy.* 4 (3), doi:10.1029/2001GC000299.
- Conrad, C. P., Husson, L., 2009. Influence of dynamic topography on sea level and its rate of change. *Lithosphere* 1 (2), 110–120, doi:10.1130/L32.1.
- Dogliani, C., Carminati, E., Bonatti, E., 2003. Rift asymmetry and continental uplift. *Tectonics* 22 (3), doi:10.1029/2002TC001459.
- Flament, N., Gurnis, M., Müller, R. D., 2013. A review of observations and models of dynamic topography. *Lithosphere* 5 (2), 189–210, doi:10.1130/L245.1.
- Flowers, R. M., Schoene, B., 2010. (U-Th)/He thermochronometry constraints on unroofing of the eastern Kaapvaal craton and significance for uplift of the southern African Plateau. *Geology* 38 (9), 827–830, doi:10.1130/G30980.1.
- Grand, S. P., 2002. Mantle shear-wave tomography and the fate of subducted slabs. *Philos. T. R. Soc. A* 360 (1800), 2475–2491, doi:10.1098/rsta.2002.1077.
- Gurnis, M., Mitrovica, J. X., Ritsema, J., van Heijst, H.-J., 2000. Constraining mantle density structure using geological evidence of surface uplift rates: The case of the African superplume. *Geochem. Geophys. Geosy.* 1 (7), doi:10.1029/1999GC000035.
- Gurnis, M., Turner, M., Bower, D., Flament, N. E., Müller, R. D., 2013. Advancing cyberinfrastructure for plate reconstructions: Present day mantle structure and the stratigraphic architecture of continents as signals of a dynamic Earth. *Geol. Soc. Am. Abstr. Programs* 45 (7).
- Gurnis, M., Turner, M., Zahirovic, S., DiCaprio, L., Spasojevic, S., Müller, R. D., Boyden, J., Seton, M., Manea, V. C., Bower, D. J., 2012. Plate tectonic reconstructions with continuously closing plates. *Comput. Geosci.* 38 (1), 35–42, doi:10.1016/j.cageo.2011.04.014.
- Hayes, D. E., 1988. Age-depth relationships and depth anomalies in the southeast Indian Ocean and South Atlantic Ocean. *J. Geophys. Res.-Sol. Ea.* 93 (B4), 2937–2954.
- Heine, C., Zoethout, J., Müller, R. D., 2013. Kinematics of the South Atlantic rift. *Solid Earth* 4 (2), 215–253, doi:10.5194/se-4-215-2013.
- Hernlund, J. W., Houser, C., 2008. On the statistical distribution of seismic velocities in Earth's deep mantle. *Earth Planet. Sc. Lett.* 265 (3), 423–437, doi:10.1016/j.epsl.2007.10.042.
- Husson, L., Conrad, C. P., Faccenna, C., 2012. Plate motions, Andean orogeny, and volcanism above the South Atlantic convection cell. *Earth Planet. Sc. Lett.* 317, 126–135, doi:10.1016/j.tecto.2011.09.001.
- Japsen, P., Chalmers, J. A., Green, P. F., Bonow, J. M., 2011. Elevated, passive continental margins: Not rift shoulders, but expressions of episodic, post-rift burial and exhumation. *Global Planet. Change* 90–91, 73–86, doi:10.1016/j.gloplacha.2011.05.004.
- Jarvis, G. T., McKenzie, D. P., 1980. Sedimentary basin formation with finite extension rates. *Earth Planet. Sc. Lett.* 48 (1), 42–52.
- Jones, S. M., White, N., Faulkner, P., Bellingham, P., 2004. Animated models of extensional basins and passive margins. *Geochem. Geophys. Geosy.* 5 (8), doi:10.1029/2003GC000658.
- Jordan, T. H., 1975. The continental tectosphere. *Rev. Geophys.* 13 (3), 1–12.
- Lay, T., Hernlund, J., Buffett, B. A., 2008. Core–mantle boundary heat flow. *Nat. Geosci.* 1 (1), 25–32, doi:10.1038/ngeo.2007.44.
- Lekic, V., French, S. W., Fischer, K. M., 2011. Lithospheric thinning beneath rifted regions of Southern California. *Science* 334 (6057), 783–787, doi:10.1126/science.1208898.
- Lithgow-Bertelloni, C., Silver, P. G., 1998. Dynamic topography, plate driving forces and the African superswell. *Nature* 395 (6699), 269–272, doi:10.1038/26212.
- Lloyd, S., van der Lee, S., França, G. S., Assumpção, M., Feng, M., 2010. Moho map of South America from receiver functions and surface waves. *J. Geophys. Res.-Sol. Ea.* 115 (B11), doi:10.1029/2009JB006829.
- Marty, J. C., Cazenave, A., 1989. Regional variations in subsidence rate of oceanic plates: A global analysis. *Earth Planet. Sc. Lett.* 94 (3), 301–315.

- Matthews, K. J., Hale, A. J., Gurnis, M., Müller, R. D., DiCaprio, L., 2011. Dynamic subsidence of Eastern Australia during the Cretaceous. *Gondwana Res.* 19 (2), 372–383, doi:10.1016/j.gr.2010.06.006.
- McKenzie, D., 1978. Some remarks on the development of sedimentary basins. *Earth Planet. Sc. Lett.* 40 (1), 25–32.
- McKenzie, D. P., 1967. Some remarks on heat flow and gravity anomalies. *J. Geophys. Res.* 72 (24), 6261–6273.
- McNamara, A. K., Zhong, S., 2004. Thermochemical structures within a spherical mantle: Superplumes or piles? *J. Geophys. Res.* 109 (B7), B07402, doi:10.1029/2003JB002847.
- Moore, A., Blenkinsop, T., Cotterill, F. W., 2009. Southern African topography and erosion history: plumes or plate tectonics? *Terra Nova* 21 (4), 310–315, doi:10.1111/j.1365-3121.2009.00887.x.
- Morgan, J. P., Smith, W. H., 1992. Flattening of the sea-floor depth-age curve as a response to asthenospheric flow. *Nature* 359, 524–527.
- Moucha, R., Forte, A. M., 2011. Changes in African topography driven by mantle convection. *Nat. Geosci.* 4 (10), 707–712, doi:10.1038/NGEO1235.
- Nyblade, A. A., Robinson, S. W., 1994. The African superswell. *Geophys. Res. Lett.* 21 (9), 765–768.
- O'Neill, C., Miller, R., Steinberger, B., 2005. On the uncertainties in hotspot reconstructions, and the significance of moving hotspot reference frames. *Geochem. Geophys. Geosy.* 6, doi:10.1029/2004GC000784.
- Ricard, Y., Richards, M., Lithgow-Bertelloni, C., Le Stunff, Y., 1993. A geodynamic model of mantle density heterogeneity. *J. Geophys. Res.-Sol. Ea.* 98 (B12), 21895–21909.
- Richter, F. M., 1973. Finite amplitude convection through a phase boundary. *Geophys. J. Int.* 35 (1-3), 265–276.
- Ritsema, J., van Heijst, H. J., Woodhouse, J. H., 1999. Complex shear wave velocity structure imaged beneath Africa and Iceland. *Science* 286 (5446), 1925–1928, doi:10.1126/science.286.5446.1925.
- Schuberth, B., Bunge, H.-P., Ritsema, J., 2009. Tomographic filtering of high-resolution mantle circulation models: Can seismic heterogeneity be explained by temperature alone? *Geochem. Geophys. Geosy.* 10 (5), doi:10.1029/2009GC002401.
- Seton, M., Müller, R., Zahirovic, S., Gaina, C., Torsvik, T., Shephard, G., Talsma, A., Gurnis, M., Turner, M., Chandler, M., 2012. Global continental and ocean basin reconstructions since 200 Ma. *Earth Sci. Rev.* 113, 212–270, doi:10.1016/j.earscirev.2012.03.002.
- Shephard, G., Liu, L., Müller, R., Gurnis, M., 2012. Dynamic topography and anomalously negative residual depth of the Argentine Basin. *Gondwana Res.* 22 (2), 658–663, doi:10.1016/j.epsl.2011.11.027.
- Shephard, G., Müller, R., Liu, L., Gurnis, M., 2010. Miocene drainage reversal of the Amazon River driven by plate-mantle interaction. *Nat. Geosci.* 3 (12), 870–875, doi:10.1038/NGEO1017.
- Simmons, N. A., Forte, A. M., Grand, S. P., 2007. Thermochemical structure and dynamics of the African superplume. *Geophys. Res. Lett.* 34 (2), doi:10.1029/2006GL028009.
- Spasojevic, S., Gurnis, M., 2012. Sea level and vertical motion of continents from dynamic earth models since the Late Cretaceous. *AAPG Bull.* 96 (11), 2037–2064, doi:10.1306/03261211121.
- Spiegel, E., Veronis, G., 1960. On the Boussinesq approximation for a compressible fluid. *Astrophys. J.* 131, 442–447.
- Stadler, G., Gurnis, M., Burstedde, C., Wilcox, L. C., Alisic, L., Ghattas, O., 2010. The dynamics of plate tectonics and mantle flow: From local to global scales. *Science* 329 (5995), 1033–1038, doi:10.1126/science.1191223.
- Steinberger, B., 2007. Effects of latent heat release at phase boundaries on flow in the Earth's mantle, phase boundary topography and dynamic topography at the Earth's surface. *Phys. Earth Planet. In.* 164 (1–2), 2–20, doi:10.1016/j.pepi.2007.04.02.
- Steinberger, B., Torsvik, T., 2008. Absolute plate motions and true polar wander in the absence of hotspot tracks. *Nature* 452, 620–623, doi:10.1038/nature06824.
- Tackley, P. J., King, S. D., 2003. Testing the tracer ratio method for modeling active compositional fields in mantle convection simulations. *Geochem. Geophys. Geosy.* 4 (4), 8302, doi:10.1029/2001GC000214.
- Thoraval, C., Richards, M. A., 1997. The geoid constraint in global geodynamics: viscosity structure, mantle heterogeneity models and boundary conditions. *Geophys. J. Int.* 131 (1), 1–8.
- Torsvik, T. H., Rousse, S., Labails, C., Smethurst, M. A., 2009. A new scheme for the opening of the South Atlantic Ocean and the dissection of an Aptian salt basin. *Geophys. J. Int.* 177 (3), 1315–1333, doi:10.1111/j.1365-246X.2009.04137.x.
- Untermeier, P., Péron-Pinvidic, G., Manatschal, G., Sutra, E., 2010. Hyper-extended crust in the South Atlantic: in search of a model. *Petrol. Geosci.* 16 (3), 207–215, doi:10.1144/1354-079309-904.
- van der Meer, D. G., Spakman, W., van Hinsbergen, D. J., Amaru, M. L., Torsvik, T. H., 2009. Towards absolute plate motions constrained by lower-mantle slab remnants. *Nat. Geosci.* 3 (1), 36–40, doi:10.1038/NGEO708.
- Wernicke, B., 1985. Uniform-sense normal simple shear of the continental lithosphere. *Can. J. Earth Sci.* 22 (1), 108–125.
- Wessel, P., Smith, W. H., 1998. New, improved version of Generic Mapping Tools released. *Eos, Trans. AGU* 79 (47), 579–579, doi:10.1029/98EO00426.
- Winterbourne, J., Crosby, A., White, N., 2009. Depth, age and dynamic topography of oceanic lithosphere beneath heavily sedimented Atlantic margins. *Earth Planet. Sc. Lett.* 287 (1), 137–151, doi:10.1016/j.epsl.2009.08.019.
- Zhang, N., Zhong, S., Flowers, R. M., 2012. Predicting and testing continental vertical motion histories since the Paleozoic. *Earth Planet. Sc. Lett.* 317, 426–435, doi:10.1016/j.epsl.2011.10.041.
- Zhang, N., Zhong, S., Leng, W., Li, Z.-X., 2010. A model for the evolution of the Earth's mantle structure since the Early Paleozoic. *J. Geophys. Res.-Sol. Ea.* 115 (B6), doi:10.1029/2009JB006896.
- Zhong, S., McNamara, A., Tan, E., Moresi, L., Gurnis, M., 2008. A benchmark study on mantle convection in a 3-D spherical shell using CitcomS. *Geochem. Geophys. Geosy.* 9 (10), Q10017, doi:10.1029/2008GC002048.

Table 1: Generic model parameters. Subscript “0” indicates reference values.

Parameter	Symbol	Value	Units
Rayleigh number	Ra	7.8×10^8	-
Thermal expansion coefficient	α_0	3×10^{-5}	K^{-1}
Density	ρ_0	4000	kg m^{-3}
Gravity acceleration	g_0	9.81	m s^{-2}
Temperature change	ΔT	1912 or 2412	K
Mantle thickness	h_M	2867	km
Thermal diffusivity	κ_0	1×10^{-6}	$\text{m}^2 \text{s}^{-1}$
Viscosity	η_0	1×10^{21}	Pa s
Chemical density (Archean lithosphere)	$\delta\rho_{ch\text{arch}}$	-1.74	%
Chemical density (Proterozoic lithosphere)	$\delta\rho_{ch\text{prot}}$	-1.52	%
Chemical density (Phanerozoic lithosphere)	$\delta\rho_{ch\text{phan}}$	-1.37	%
Earth radius	R_0	6371	km
Activation energy (upper mantle)	$E_{\eta\text{UM}}$	100	kJ mol^{-1}
Activation energy (lower mantle)	$E_{\eta\text{LM}}$	33	kJ mol^{-1}
Activation temperature	T_η	452	K
Compositional viscosity pre-factor	η_C	100	-
Background mantle temperature	T_b	1685	K

Table 2: Case-specific parameters

Case ^a	Input							Output
	$\eta_0(r)$ ^b	T_{cmb} [K]	$\eta(T)$	Γ	z_{slab}^l [km]	$\delta\rho_{ch\text{cc}}$	$\delta\rho_{ch\text{cmb}}$	$\Delta H_{\text{K-SF}}$ [m] ^c
TC1	1,1,1,1,100	2185	Y	N	1750	-7.97 %	N	750 ± 408
TC1R	1,1,1,1,100	2185	Y	N	1750	-8.63 %	N	783 ± 400
TC2	1,1,1,1,75	2185	Y	N	1750	-7.97 %	N	703 ± 398
TC3	1,1,1,1,50	2185	Y	N	1750	-7.97 %	N	647 ± 407
TC4	1,1,1,5,50	2185	Y	N	1750	-7.97 %	N	487 ± 406
TC5	1,1,1,1,50	2185	N	N	1750	-7.97 %	N	545 ± 440
TC6	1,1,1,1,100	2185	Y	Y	1750	-7.97 %	N	633 ± 405
TC7	1,1,1,1,10 → 100	2185	Y	N	1750	-7.97 %	N	570 ± 421
TC8	1,1,1,1,10 → 50	2185	Y	N	1750	-7.97 %	N	477 ± 452
TC9	1,1,1,1,10 → 30	2185	Y	N	1750	-7.97 %	N	418 ± 458
HC1	1,1,1,1,100	2185	Y	N	1750	-7.97 %	N	691 ± 414
HC2	1,1,1,1,40	2185	Y	N	1750	-7.97 %	N	600 ± 426
HH1	1,1,1,1,100	2685	Y	N	1750	-7.97 %	+ 3.6 %	429 ± 438
HH1R	1,1,1,1,100	2685	Y	N	1750	-8.63 %	+ 3.6 %	589 ± 341
HH2	1,1,1,1,100	2685	Y	N	1210	-7.97 %	+ 3.6 %	492 ± 422
HH3	1,0,1,1,100	2685	Y	N	1750	-7.97 %	+ 3.6 %	672 ± 368

^a Txx indicates cases based on the South Atlantic reconstruction of Torsvik et al. (2009), Hxx based on that of Heine et al. (2013), xCx “cold” CMB, xHx “hot” CMB and xxxR cases restarted at 150 Ma

^b Values of the pre-factor in Eq. 8 for mantle above 160 km, between 160-310 km, between 310-410 km, below 410 km, and below 670 km. The “→” symbol indicates that the viscosity linearly increases with depth between the two listed values.

^c Elevation difference between the Kaapvaal and São Francisco cratons. For ETOPO1 (Amante and Eakins, 2009), $\Delta H_{\text{K-SF}} = 406 \pm 455$ m.

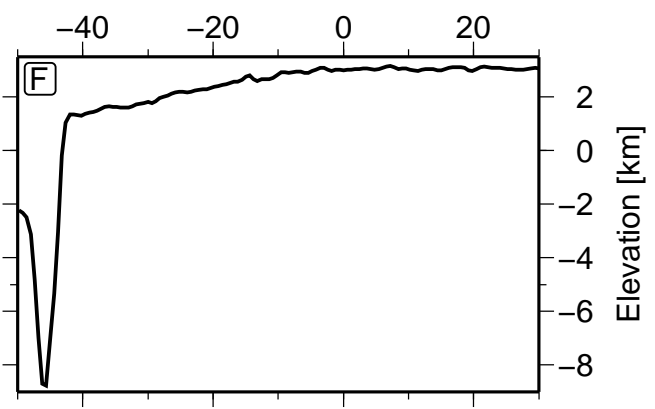
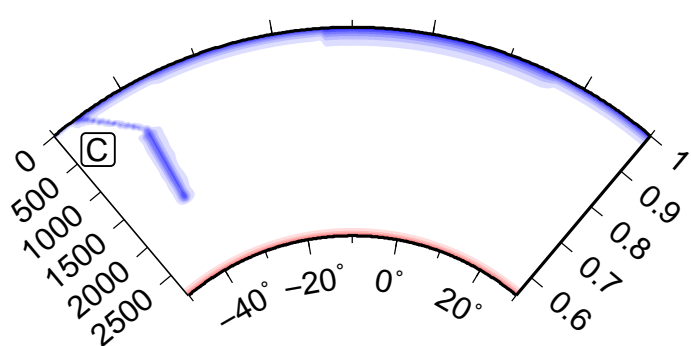
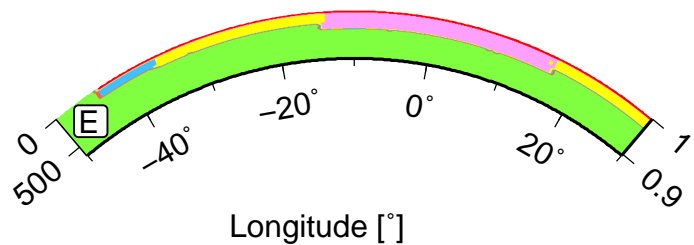
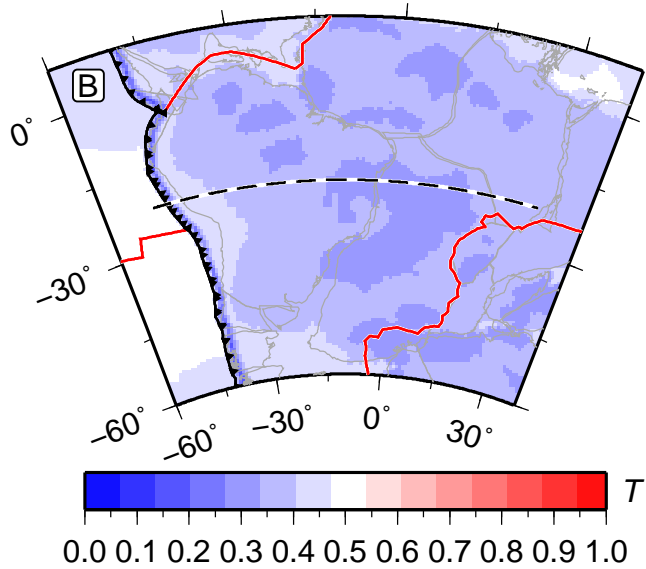
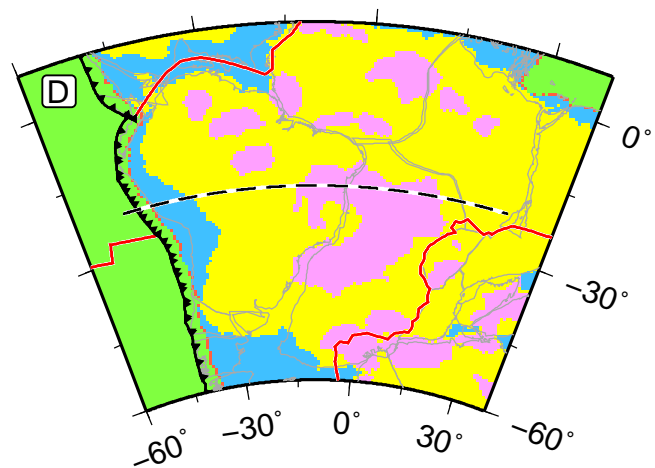
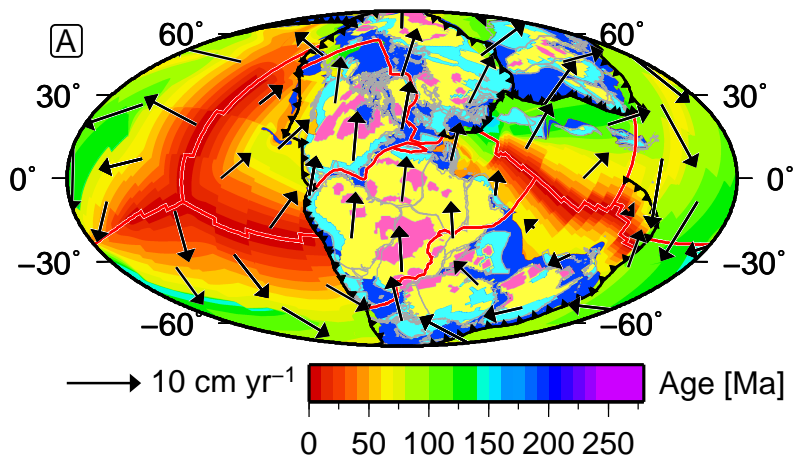


Figure 1: (*Previous page*) Data assimilated and initial conditions for case HH1. A. Plate velocities, age of the ocean floor and tectonothermal age of the continents, the latter simplified from Artemieva (2006). The colour palette refers to oceanic ages. Continents of Archean age are pink, Proterozoic yellow, Phanerozoic cyan and inferred continental material in dark blue. Mid-ocean ridges and transform faults are shown in red, subduction zones in black with triangles on the overriding plate, and present-day coastlines in grey. Mollweide projection. B. Initial non-dimensional temperature at 109 km depth for western Pangea. Albers projection with two standard parallels at 14°S and 37°S. C. Whole mantle cross-section at 22°S (dashed black line in B and D) of the initial mantle temperature. Left axis shows depth in km and right axis non-dimensional radius. D. Initial composition at 109 km depth. E. Upper mantle cross section at 22°S showing the vertical distribution of the four compositionally distinct tracer types. F. Initial topography at 22°S, air-loaded in the continents and water-loaded in the oceans. The continent is isostatically flat but dynamically tilted towards the trench.

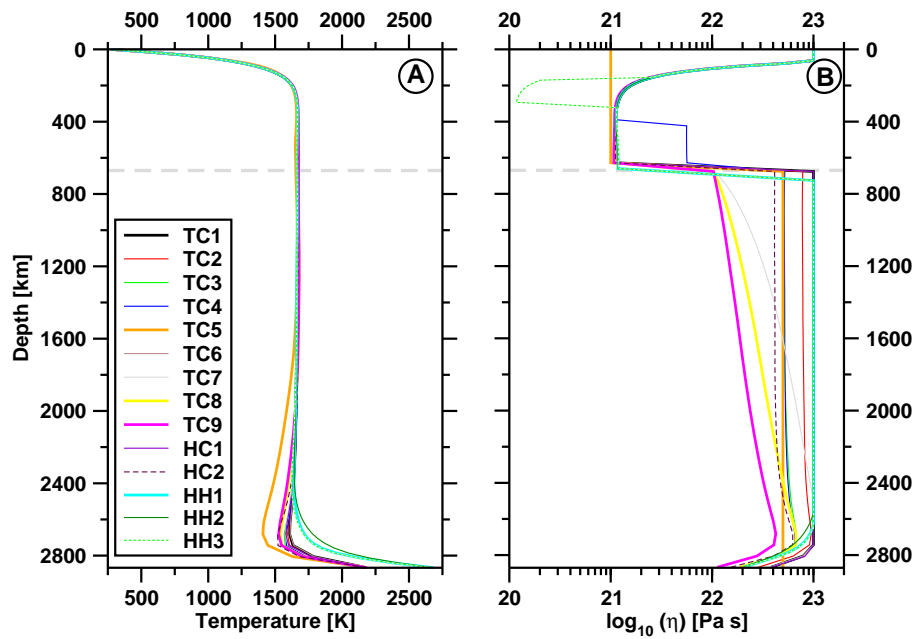


Figure 2: Present-day horizontal-average temperature profiles obtained for each case (A), and resulting temperature-dependence of viscosity (B). See Table 2 for case-specific parameters. The dashed grey line is the upper-lower mantle boundary.

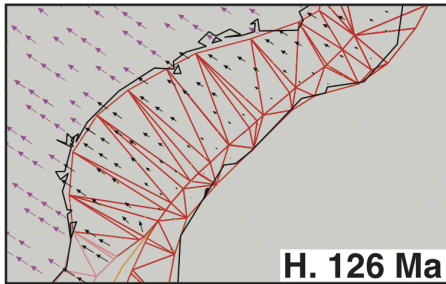
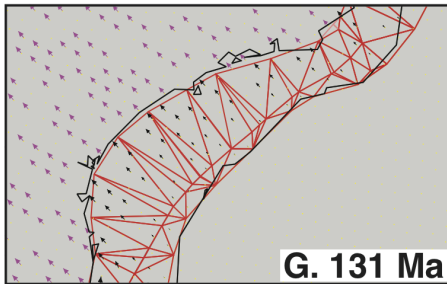
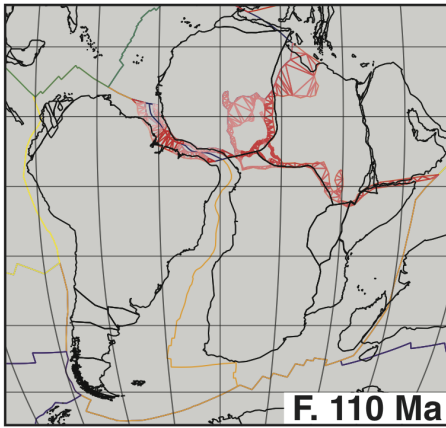
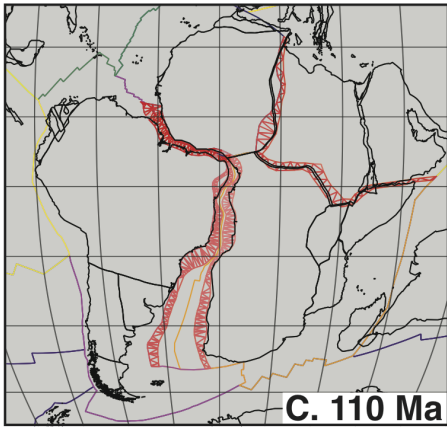
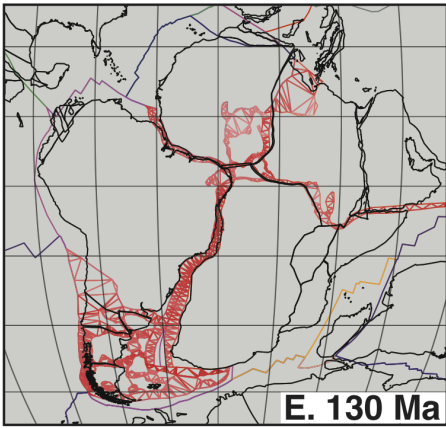
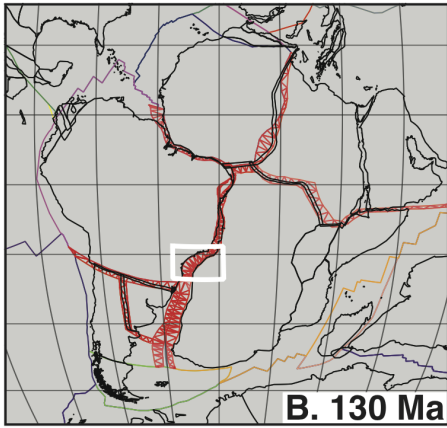
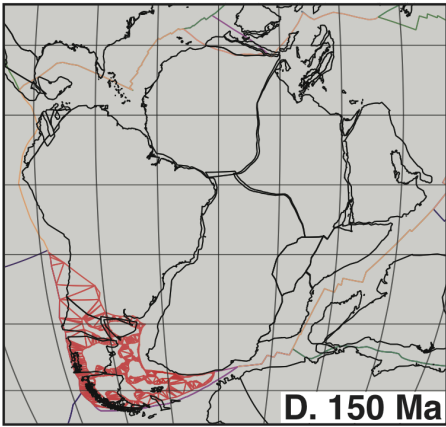
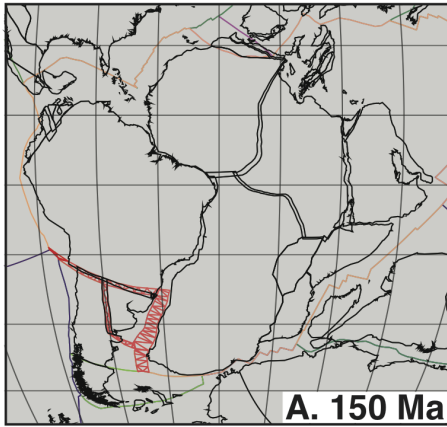


Figure 3: (*Previous page*) South Atlantic reconstructions with deforming plate boundary zones. Reconstructed present-day coastlines are shown in black, plate boundaries are coloured according to plate identities, and deforming meshes are coloured according to the second invariant of the incremental strain rate, with darker reds showing faster deformation (Gurnis et al., 2013). The reconstruction of Torsvik et al. (2009) is shown on the left and that of Heine et al. (2013) on the right at 150 Ma (A and D), 130 Ma (B and E) and 110 Ma (C and F). Robinson projection with graticules 15 degrees apart. The velocity field with Africa fixed and the *CitcomS* mesh (yellow dots) are shown for the white area in B at 131 Ma (G) and 126 Ma (H).

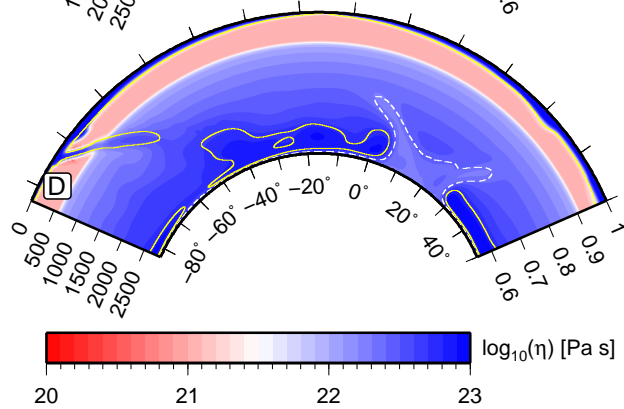
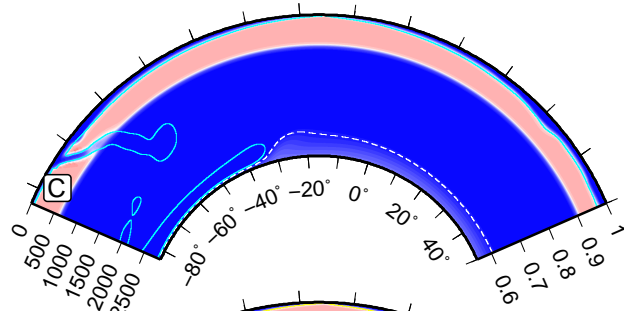
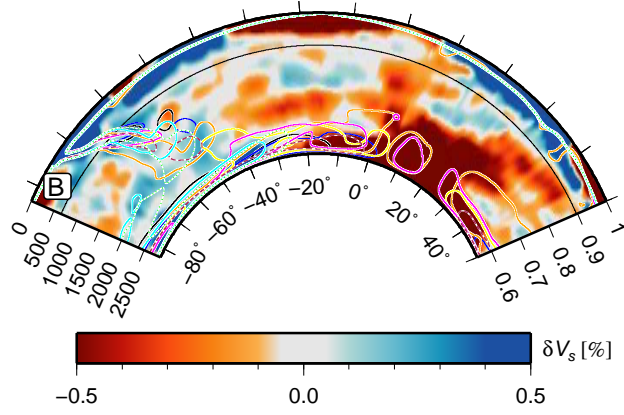
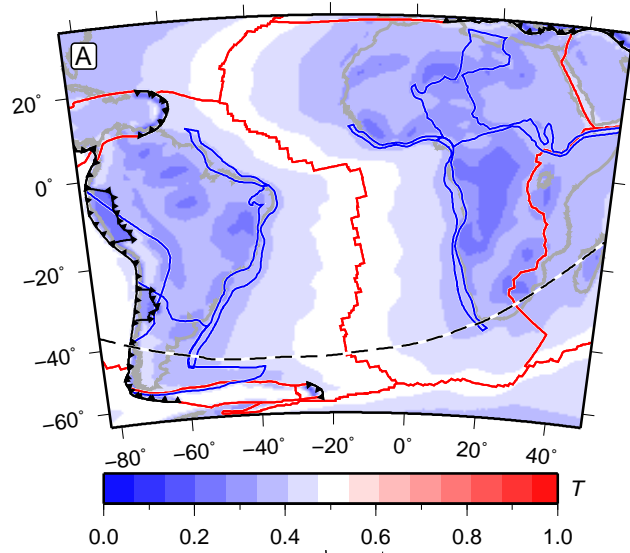


Figure 4: (*Previous page*) Predicted present-day temperature and viscosity. A. Predicted present-day temperature at 109 km depth for case HH1. The blue polygons show areas that have undergone deformation in which there is no assimilation and other lines are as in Fig. 1. Albers projection with two standard parallels at 26°S and 12°N. B. Whole-mantle cross-section through a *S*-wave tomography model (Grand, 2002) along South Atlantic flowline at 45°S (see A), with contours of mantle 10% colder than ambient overlain for cases TC1, TC4, TC5, TC8, TC9, HC2, HH1 and HH3 (colour coding as in Fig. 2). C-D. Model viscosity for cases HH1 (C) and TC8 (D) with dashed-white contours of mantle 10% hotter than ambient.

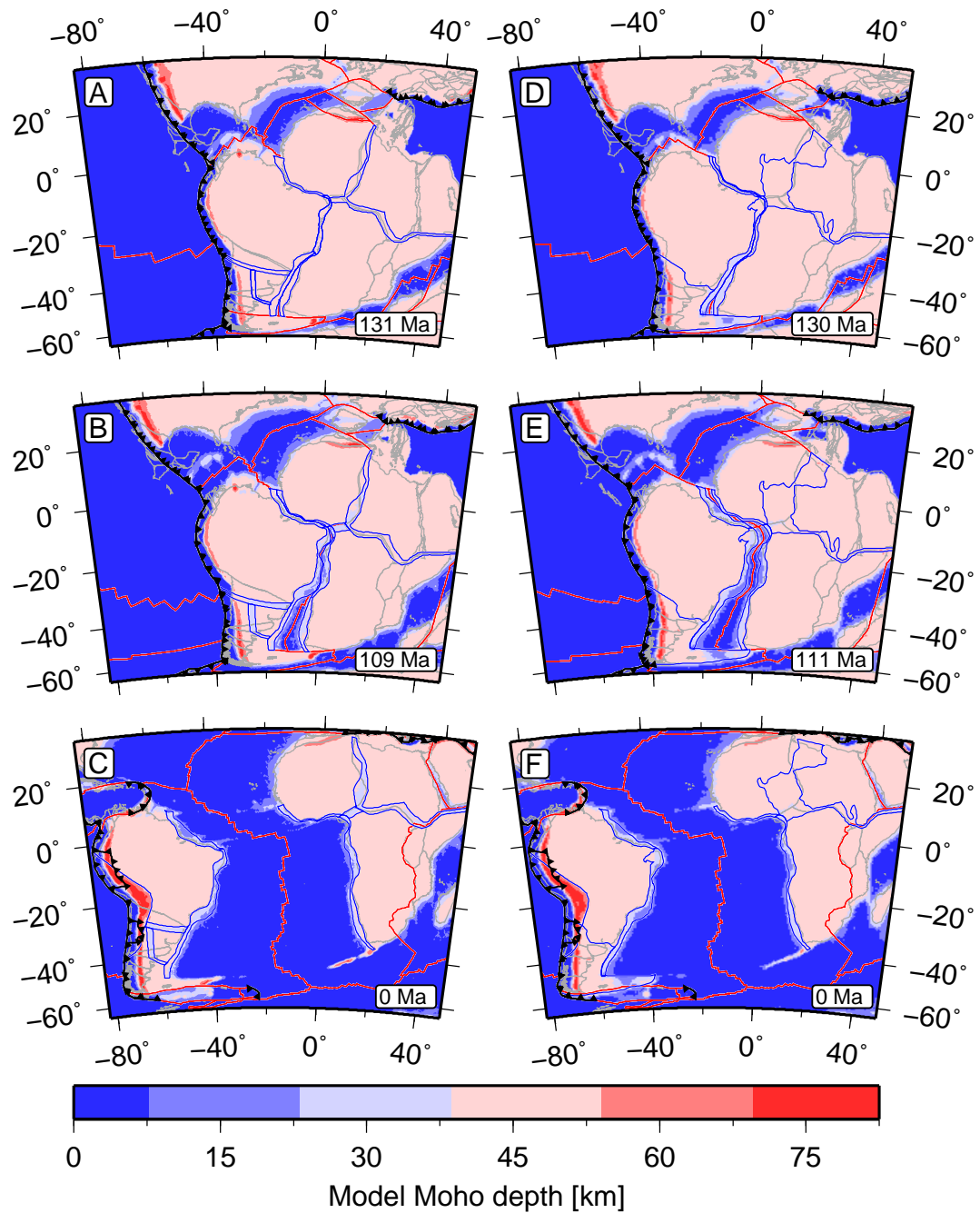


Figure 5: Predicted evolution of continental crustal thickness for case TC1 based on the reconstruction of Torsvik et al. (2009), left and case HH1 based on the reconstruction of Heine et al. (2013), right, at ~ 130 Ma (A and D), ~ 110 Ma (B and E) and present-day (C and F). Projection and lines as in Fig. 4 A.

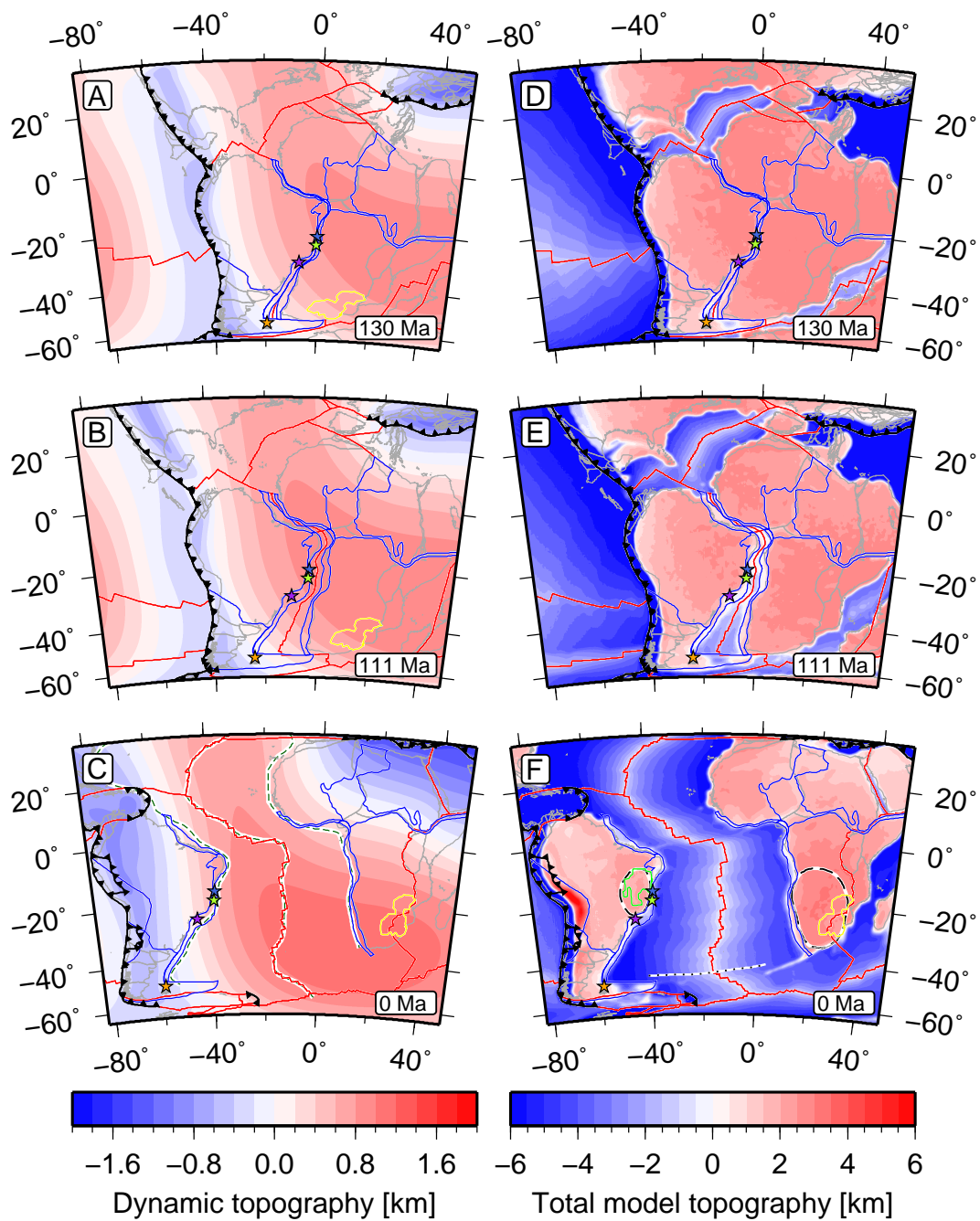


Figure 6: (*Previous page*) Predicted evolution of air-loaded dynamic topography (left) and total topography (right, air-loaded continents and water-loaded oceans) for case HH1 at 130 Ma (A and D), 111 Ma (B and E) and present-day (C and F). See Supplementary Animation for the dynamic topography in 10 Myr increments since 150 Ma. Projection and lines as in Fig. 4 A. The coloured stars are boreholes for which tectonic subsidence is available (Fig. 8). The outline of the Kaapvaal Craton (Artemieva, 2006) is shown in yellow, and that of the Sao Francisco Craton in green (F). Southern part of the transects along which residual topography is estimated (Winterbourne et al., 2009, Fig. 10) are shown as dashed green lines over thick white lines in C; see Fig. 2 of Winterbourne et al. (2009) for full extent of these transects. In F, the dotted black line is a South Atlantic flowline at 45°S for oceanic ages < 83.6 Ma (start of Cretaceous normal superchron), and the dashed black outlines are the approximate, minimum extent of the Brazilian and southern African plateaus.

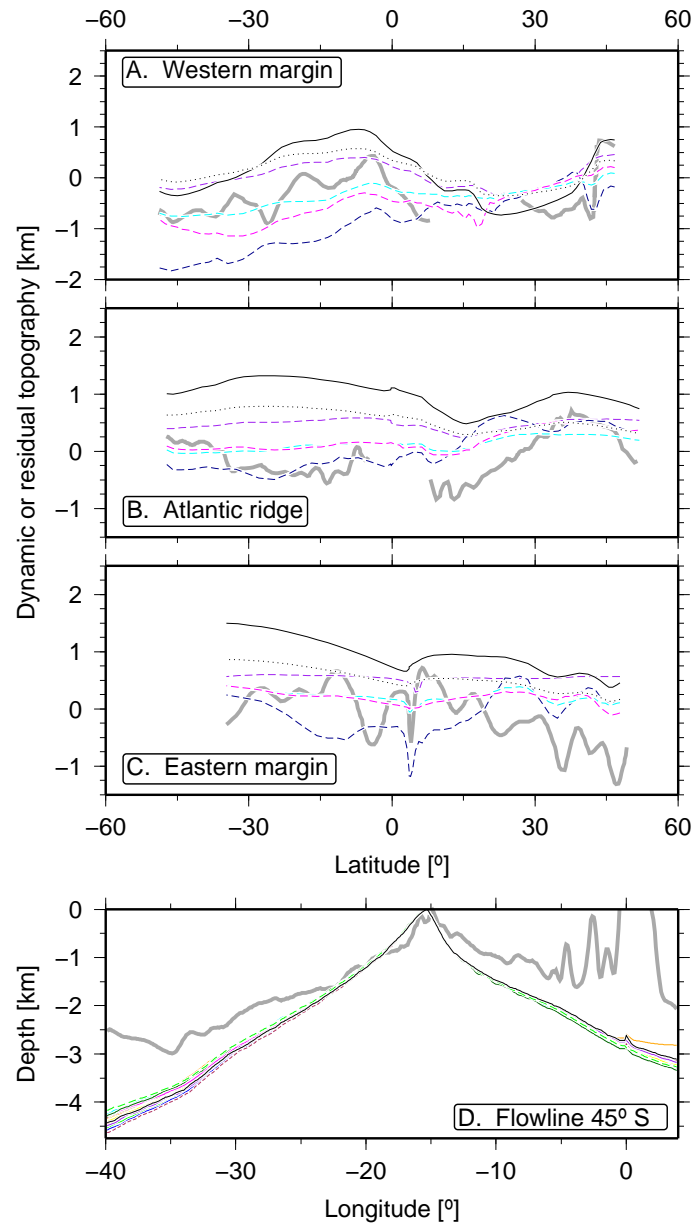


Figure 7: A-C. Predicted present-day water-loaded dynamic topography for case TC1 (solid black line for no-slip surface and dotted line for free-slip surface) and for the models of Ricard et al. (1993, dashed purple line), Steinberger (2007, dashed blue line), Conrad and Husson (2009, dashed cyan line) and Spasojevic and Gurnis (2012, dashed magenta line), and residual topography derived from long-wavelength gravity (thick grey lines from Fig. 10 of Winterbourne et al., 2009) along the margins and the mid-oceanic ridge of the Atlantic ocean. See Fig. 6C for location of the southern part of these transects and Fig. 2 of (Winterbourne et al., 2009) for complete transects. D. Predicted total model topography for all cases (colour coding as in Fig. 2) and ETOPO1 topography sampled along the flowline shown in Fig. 6F, similar to the transect considered by Morgan and Smith (1992). The topography was smoothed using a Gaussian filter of wavelength 100 km.

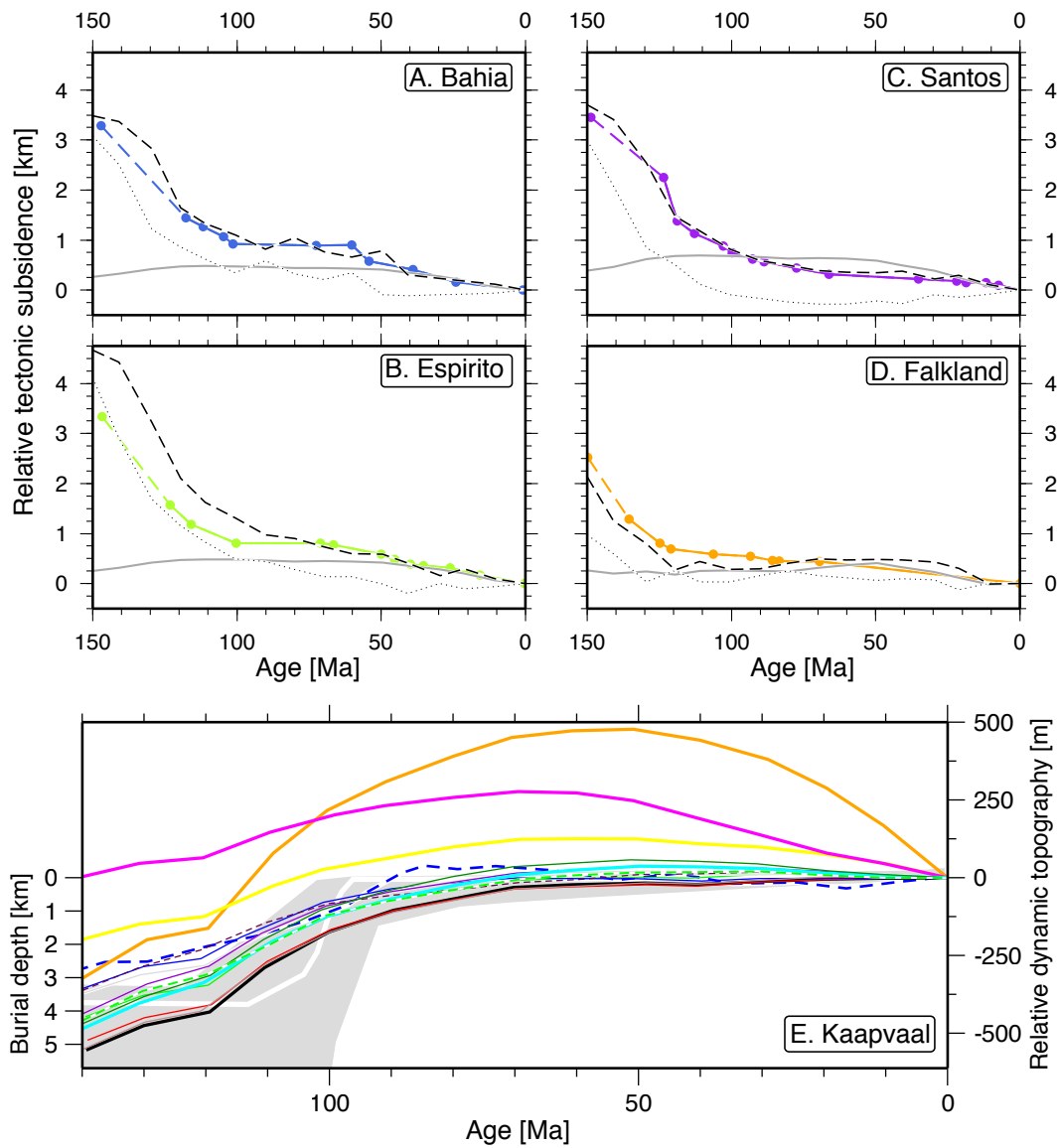


Figure 8: A-D. Comparison between observed (solid coloured dotted lines) and predicted (case HC1, dashed black lines) tectonic subsidence for four South Atlantic boreholes (see coloured stars in Fig. 6). The contribution of dynamic topography (*e.g.* Fig. 6A-C) is shown as grey lines, and the difference between total topography and dynamic topography is shown as black dotted lines. E. Predicted evolution of dynamic topography for all cases (colour coding as in Fig. 2) and for the model of Zhang et al. (2012, dashed thick blue line), and uplift history of the Kaapvaal as constrained from thermochronological data and models (thick white line and grey field) as in Zhang et al. (2012).

Supplementary material for
Topographic asymmetry of the South Atlantic from
global models of mantle flow and lithospheric stretching

Flament et al.

Earth and Planetary Science Letters

1. Kinematic models for deforming regions

The methodology for building deforming regions into global plate reconstructions builds on the continuously closing plates framework described by Gurnis et al. (2012). Plates are defined within the open-source software *GPlates* (Boyden et al., 2011) by building polygons from a series of lines defining plate boundaries. The lines can move independently, so that the geometry of plate polygons continually change as a function of reconstruction time. Within this original framework, plate velocities within each plate polygons were based on the stage rotation of that plate (*i.e.* plates were considered internally ‘rigid’, but with crust being accreted or destroyed at the plate boundaries).

The kinematic models used in this paper use an adaptation of the continuously closing plates methodology to allow deformation within certain regions. Similar to the original continuously closing plates concept, the boundaries of deforming regions are built within *GPlates* from a series of lines and points. These lines and points have their own motion history such that the deforming regions can change geometry over time. However, within deforming regions, the plate velocities are not calculated from a single stage pole - instead, they

are derived by interpolation of velocities from points on the boundaries of the deforming regions, as well as additional constraints within the deforming zones (lines, points or smaller ‘rigid’ polygons) whose motion is constrained by geological observation. Figs. 1 and 2 show the regions of deformation within our model - the methodology used to delineate the extent of these regions is also discussed in Section 2.4 of the main text.

For example, our models incorporate a representation of deformation within the Andes from 45 Ma to present day. The kinematic model, covering the area shown by the green hatching in Figs. 1 and 2, is based on the study of Arriagada et al. (2008), who derived 2D map restorations of the central Andes using a combination tectonic shortening estimates and paleomagnetic rotations. In our reconstructions, a series of points within individual motion histories are defined both along the Andean margin and within the region of Andean crustal shortening, providing a representation both of crustal shortening and the changing geometry of the Andean convergent margin.

A different approach is required for conjugate passive margins. For these regions, we use a method similar to that described by Srivastava and Verhoeve (1992). To construct kinematic models of margin extension and breakup that remain topologically correct for all reconstruction times, we first define the extent of extended continental crust within each margin. We start with a set of continent-ocean boundaries (COBs) on the conjugate margins and a series of finite rotations that describes the relative motion between the plate-pair (for example, rotations between South America and Southern Africa) beginning from the onset of rifting. Given this information, we can create a set of vertices on the conjugate COB lines that map onto each other during

the reconstruction. Each vertex on each COB has an individual motion history. The motion history is derived from the combination of geometries and finite rotations, so that topological correctness is preserved at all times. For times when ‘rigid’ COBs would imply overlap between the conjugate margins, COB points move along small circle paths defined by the stage pole of the rigid plate pair. The magnitude of the motion is calculated to preserve the present-day ratio of the widths of the conjugate margins. Following this method, we can derive a kinematic model that describes progressive breakup and onset of seafloor spreading. For example, Figs. 3C and F (main text) show a stage in the South Atlantic where breakup has already occurred in the southern South Atlantic (so plate velocities here are consistent with the stage pole for South America), while extension continues in the Equatorial Atlantic and plate velocities within the deforming regions are derived by linear interpolation from the surrounding constraints.

Definition of deforming regions is more straightforward for regions within Africa and South America where rifting did not proceed to breakup. In both the models tested here the African continent comprises rigid blocks separated by regions of deformation that correspond to fairly well known rift basins which formed contemporaneously with South Atlantic opening (see Torsvik et al., 2009 and Heine et al., 2013 for further discussion). Cretaceous deformation within South America in both models is confined to the southern part of the continent. In the case of the Torsvik et al. (2009) model, the extent of the areas affected by extension and oblique transtension between the Colorado, Paraná and Amazonia blocks is not explicitly illustrated, and additional data to define the extent of these basins is lacking. We have

defined regions ~ 150 km wide to accommodate this deformation.

2. Model equilibrium

To assess the state of the model from the initial condition at 200 Ma, we follow the evolution of average CMB heat flux and minimum dynamic topography. These two quantities are expected to be initially furthest away from equilibrium because the temperature field is synthetic with imposed subduction zones that correspond to dynamic topography lows.

2.1. Average core-mantle boundary heat flux

Fig. 3 shows that CMB heat flux is initially not in equilibrium for all cases. A thermal boundary layer was not included in the initial condition for cold cases, for which CMB heat flux initially increases sharply between 200-190 Ma. CMB heat flux then steadily decreases, and increases again as cold material reaches the CMB. This arrival occurs sooner in less viscous cases (see coloured tick marks on Fig. 3), and it precedes the minimum value of CMB heat flux by ~ 10 -25 Myr. This minimum is reached later in the model run (~ 100 Ma) for the more viscous cases, and earlier (between ~ 165 -150 Ma) for the less viscous cases. Hot cases reach a minimum CMB heat flux by 150 Ma, following an initial decrease. For case HH2, the CMB heat flux does not increase again, which could indicate that the amount of cold material initially inserted in the lower mantle for this case is closer to dynamic equilibrium for the assumed Rayleigh number. For low-viscosity cases, the CMB heat flux appears to oscillate around equilibrium from the first minimum, with a period $\gtrsim 160$ Myr. However, high-viscosity cases show little CMB heat flux variation in the last 50 Myr. Taking the dynamic

thermal equilibrium as the half-amplitude of the oscillations, and assuming these would carry on beyond present-day for all cases, hot (cold) cases have been within $\sim 8\%$ ($\sim 15\%$) of equilibrium since CMB heat flux reached a minimum.

2.2. Minimum dynamic topography

Fig. 4 shows that all cold cases and case HH1 are initially not in equilibrium for minimum surface dynamic topography that generally decreases between 200-180 Ma, then increases between 180-140 Ma and then plateaus, indicating that equilibrium has been reached, to the exception of case TC5 (temperature-independent viscosity) that does not reach equilibrium until ~ 70 Ma. Case HH2 (shallower slabs in the initial condition) and case HH3 (low-viscosity asthenosphere) are initially closer to equilibrium for minimum dynamic topography and show less pronounced re-adjustments towards equilibrium.

References

- Arriagada, C., Roperch, P., Mpodozis, C., Cobbold, P., 2008. Paleogene building of the Bolivian Orocline: Tectonic restoration of the central Andes in 2-D map view. *Tectonics* 27 (6), doi:10.1029/2008TC002269.
- Bouysse, P., Palfreyman, D., 2000. Geological Map of the World at 1:25 M. Commission for the Geological Map of the World.
- Boyden, J. A., Müller, R. D., Gurnis, M., Torsvik, T., Clark, J. A., Turner, M., Ivey-Law, H., Watson, R. J., Cannon, J., 2011. Next-generation plate-

- tectonic reconstructions using GPlates. *Geoinformatics: Cyberinfrastructure for the Solid Earth Sciences*, 95–114.
- Divins, D., 2003. Total Sediment Thickness of the World's Oceans and Marginal Seas. NOAA National Geophysical Data Center, Boulder, CO.
- Gurnis, M., Turner, M., Zahirovic, S., DiCaprio, L., Spasojevic, S., Müller, R. D., Boyden, J., Seton, M., Manea, V. C., Bower, D. J., 2012. Plate tectonic reconstructions with continuously closing plates. *Comput. Geosci.* 38 (1), 35–42, doi:10.1016/j.cageo.2011.04.014.
- Heine, C., Zoethout, J., Müller, R. D., 2013. Kinematics of the South Atlantic rift. *Solid Earth* 4 (2), 215–253, doi:10.5194/se-4-215-2013.
- Montelli, R., Nolet, G., Dahlen, F., Masters, G., 2006. A catalogue of deep mantle plumes: new results from finite-frequency tomography. *Geochem. Geophys. Geosy.* 7 (11), Q11007, doi:10.1029/2006GC001248.
- Ritsema, J., van Heijst, H. J., Woodhouse, J. H., 1999. Complex shear wave velocity structure imaged beneath Africa and Iceland. *Science* 286 (5446), 1925–1928, doi:10.1126/science.286.5446.1925.
- Sandwell, D. T., Smith, W. H., 2009. Global marine gravity from retracked Geosat and ERS-1 altimetry: Ridge segmentation versus spreading rate. *J. Geophys. Res.-Sol. Ea.* 114 (B1), doi:10.1029/2008JB006008.
- Simmons, N. A., Forte, A. M., Boschi, L., Grand, S. P., 2010. GyPSuM: A joint tomographic model of mantle density and seismic wave speeds. *J. Geophys. Res.-Sol. Ea.* 115 (B12), doi:10.1029/2010JB007631.

- Srivastava, S., Verhoef, J., 1992. Evolution of Mesozoic sedimentary basins around the North Central Atlantic: a preliminary plate kinematic solution. *Geol. Soc., London, S.P.* 62 (1), 397–420.
- Torsvik, T. H., Rouse, S., Labails, C., Smethurst, M. A., 2009. A new scheme for the opening of the South Atlantic Ocean and the dissection of an Aptian salt basin. *Geophys. J. Int.* 177 (3), 1315–1333, doi:10.1111/j.1365-246X.2009.04137.x.
- Winterbourne, J., Crosby, A., White, N., 2009. Depth, age and dynamic topography of oceanic lithosphere beneath heavily sedimented Atlantic margins. *Earth Planet. Sc. Lett.* 287 (1), 137–151, doi:10.1016/j.epsl.2009.08.019.

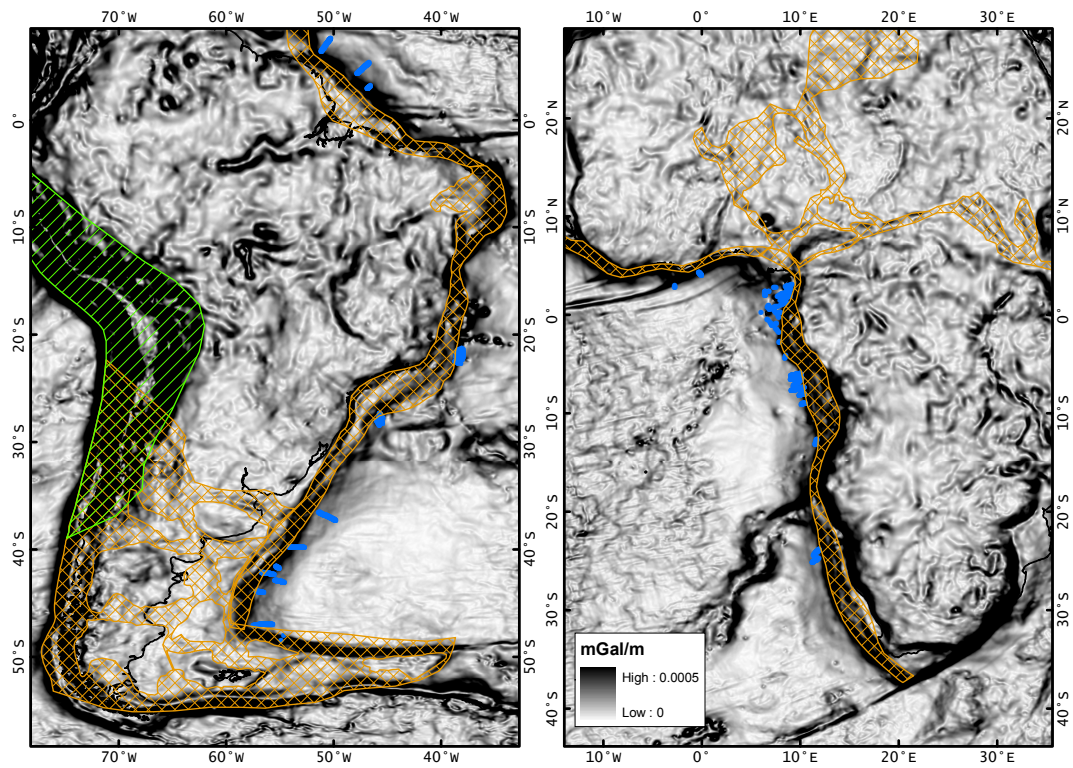


Figure 1: Total horizontal gradient of the 20 km upward continued Bouguer gravity. The landward limit of extended crust is defined to lie along the landward edge of large horizontal gradients. Regions within the orange hatched areas (here shown for the kinematic model of Heine et al., 2013) underwent deformation during Cretaceous South Atlantic opening. Green hatched region shows the extent of Cenozoic shortening in the Andes (adapted from Arriagada et al., 2008). Blue dots show extent of *bona fide* oceanic crust interpreted from seismic profiles by Winterbourne et al. (2009).

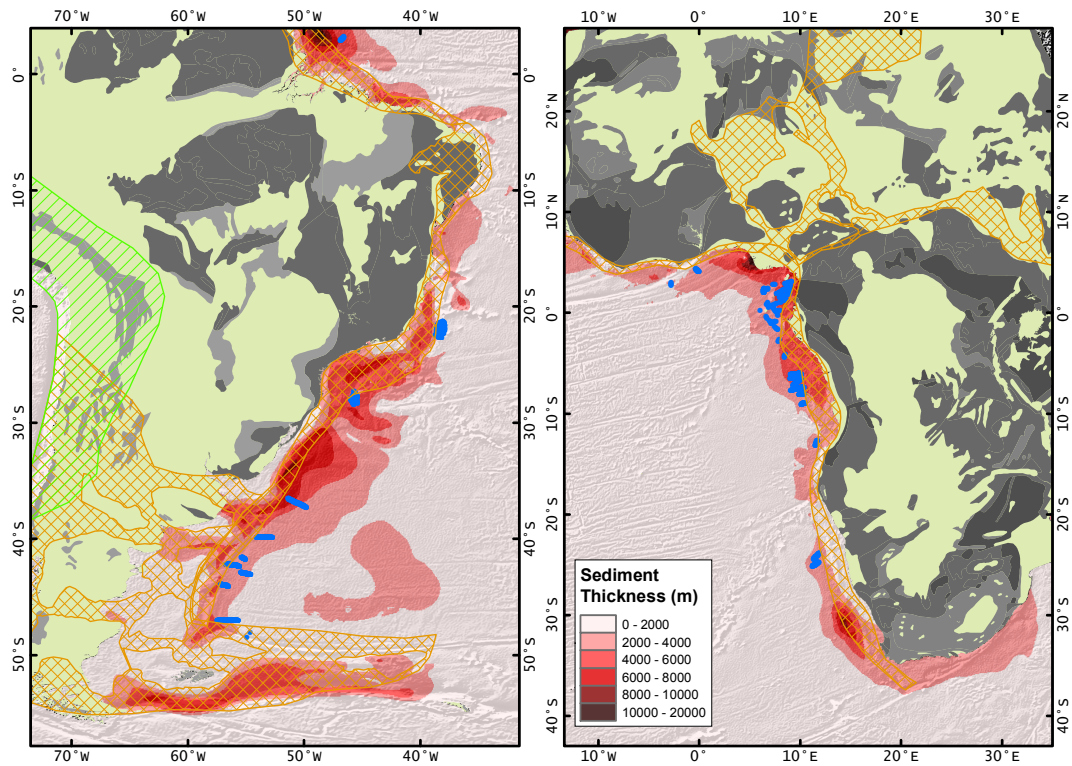


Figure 2: Offshore, the sediment thickness (Divins, 2003) is shown as shades of red, and the texture is derived from the gradient of free-air gravity anomalies based on satellite altimetry (Sandwell and Smith, 2009). Onshore, the surface geology (simplified from Bouysse and Palfreyman, 2000) is shown as shades of grey, with the light grey representing Paleozoic units and darker greys representing Proterozoic and Archean units. Deforming areas and *bona fide* oceanic crust are shown as in Supplementary Fig. 1.

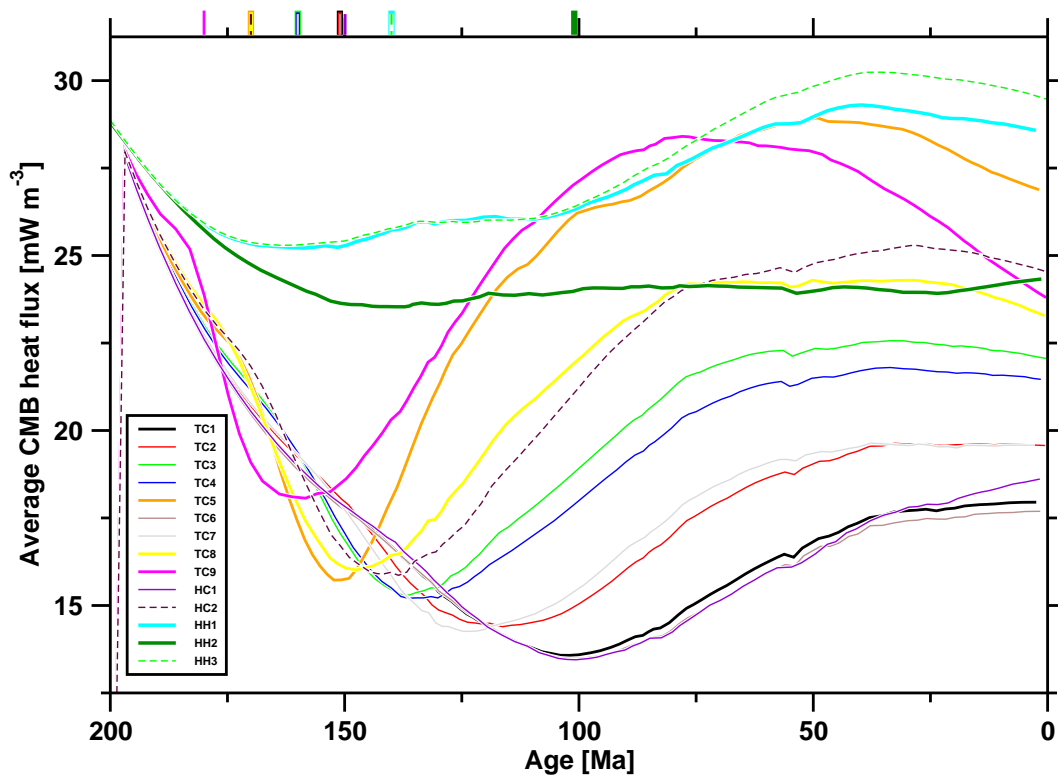


Figure 3: Evolution of average core-mantle-boundary heat flux for all cases. The tick marks at the top, coloured by model, indicate the first occurrence of cold material at ~ 2810 km depth, detected visually.

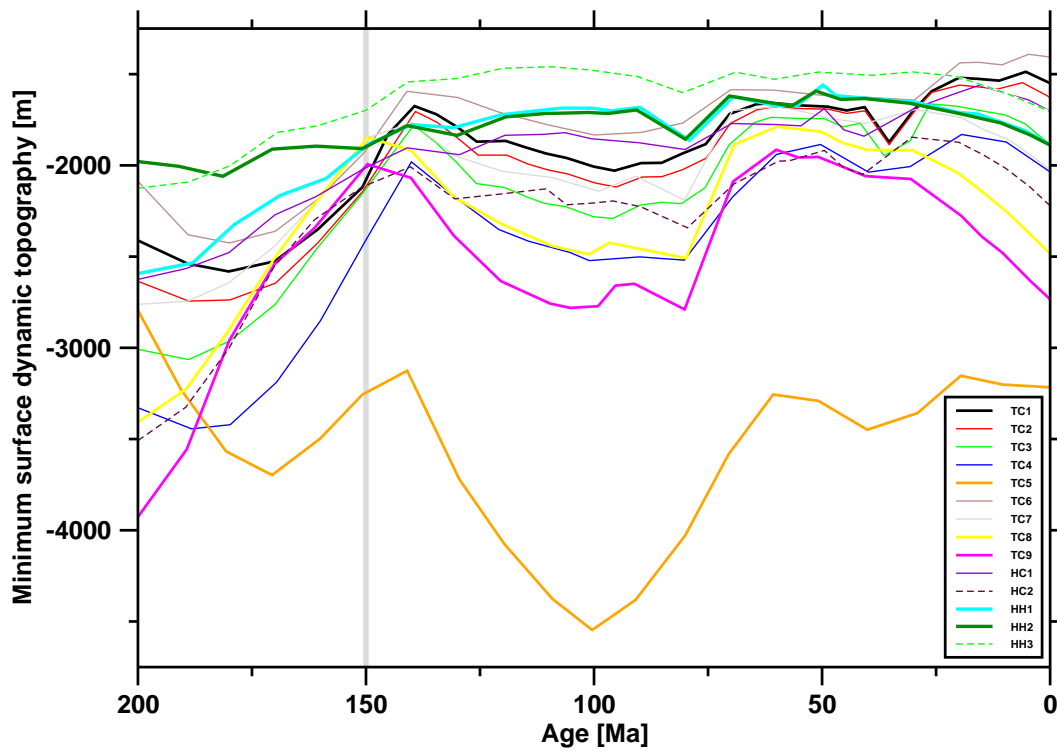


Figure 4: Evolution of minimum dynamic topography for all cases. The grey vertical line at 150 Ma indicates the age from which dynamic topography results are presented.

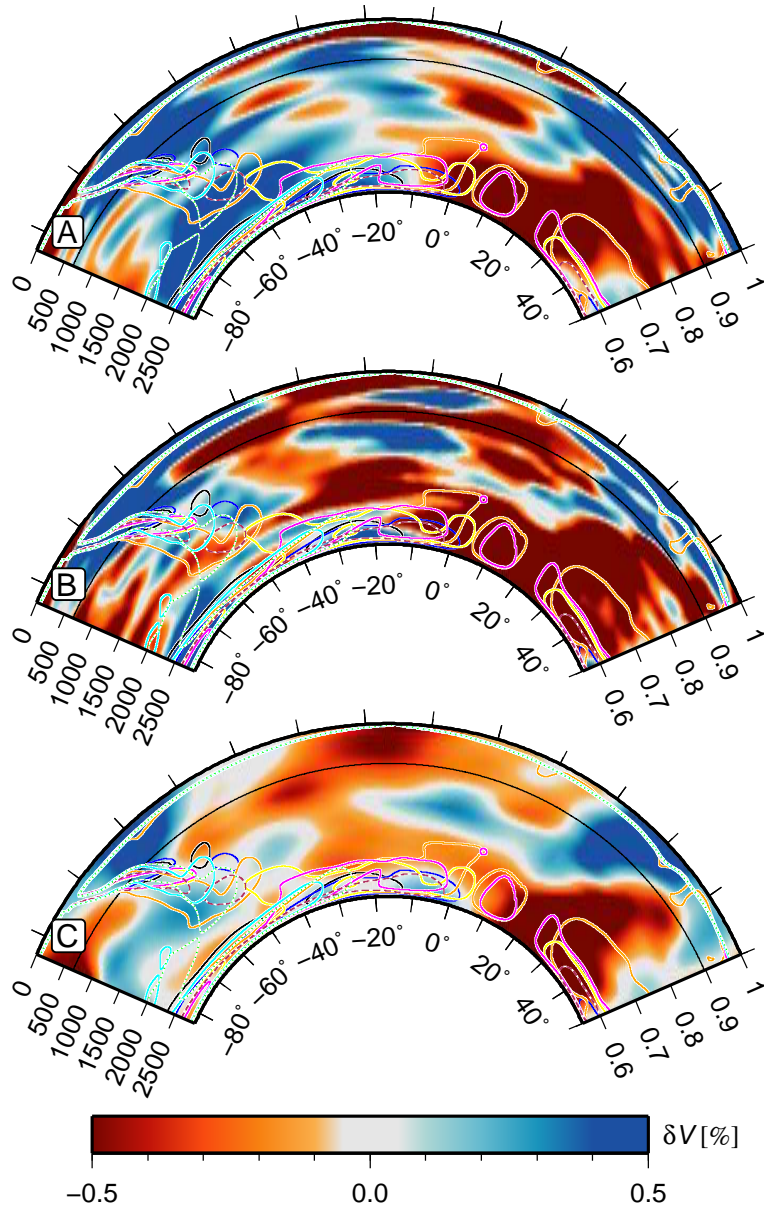


Figure 5: As Fig. 4B of the main text, for tomography A. *S*-wave model S20RTS (Ritsema et al., 1999), B. *S*-wave model GyPSuM (Simmons et al., 2010) and C. *P*-wave model of Montelli et al. (2006).

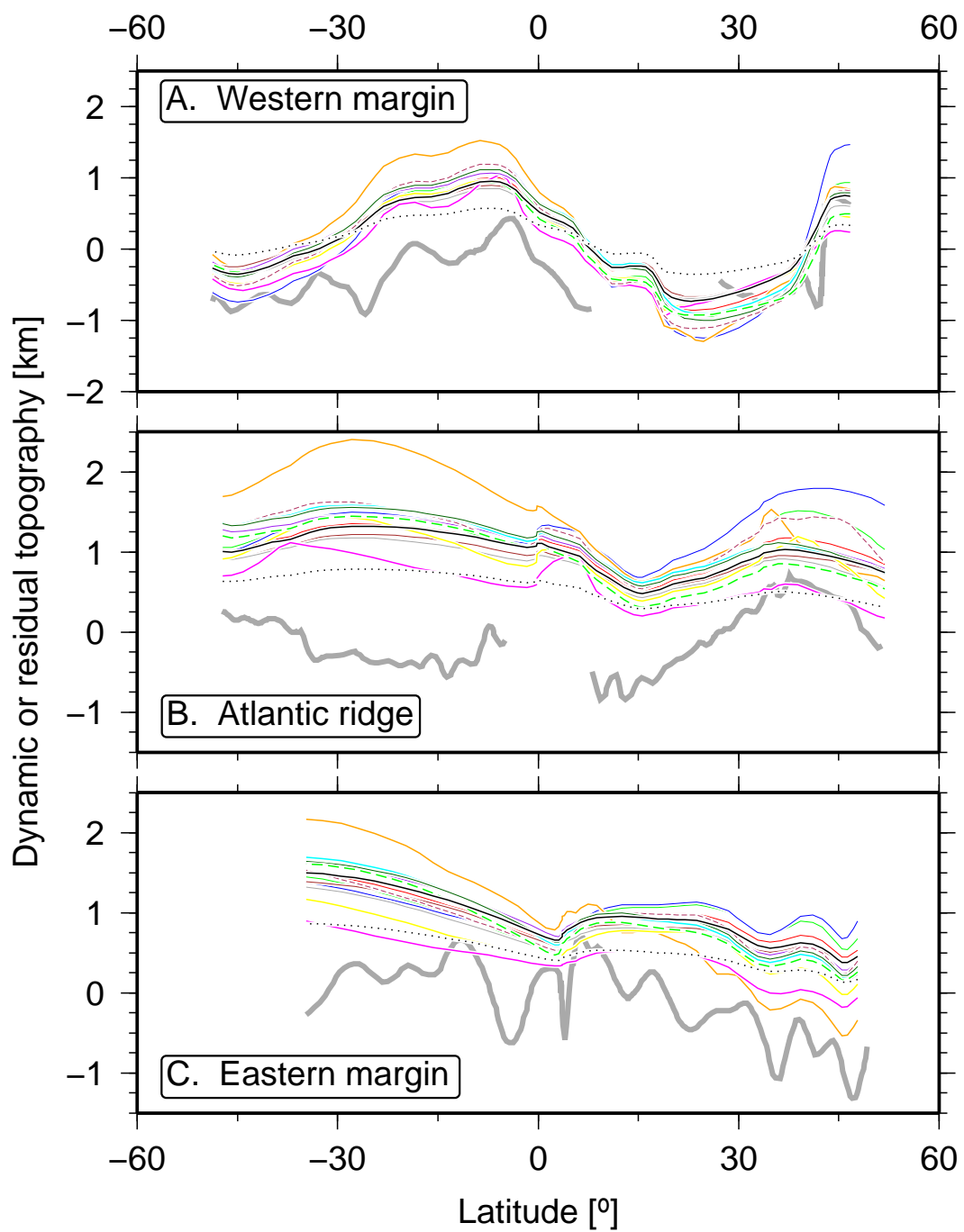


Figure 6: As Fig. 7A-C of the main text, for all modelled cases.

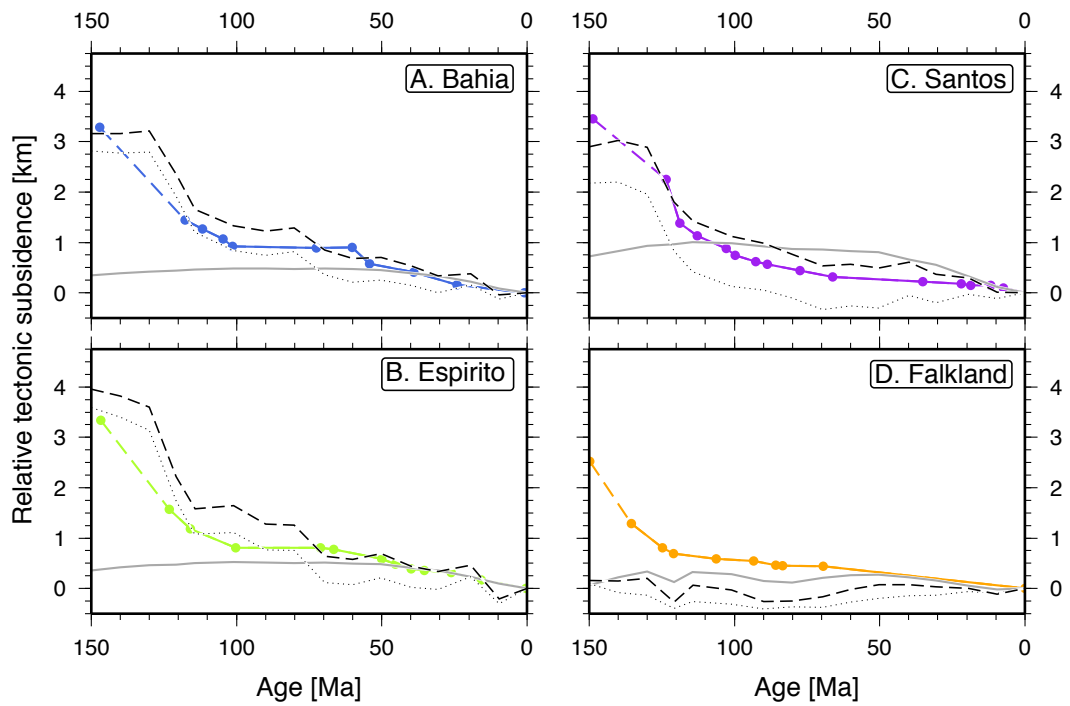


Figure 7: As Fig. 8A-D of the main text, for case TC4. The North Falkland basin is south of the deforming zone based on the reconstruction of Torsvik et al. (2009), therefore stretching is not predicted at that location.